Remote Sensing of Environment 215 (2018) 284–299

Contents lists available at ScienceDirect

Remote Sensing of Environment

journal homepage: www.elsevier.com/locate/rse

Developing a composite daily snow cover extent record over the Tibetan Plateau from 1981 to 2016 using multisource data

Xiaona Chen[a], Di Long[a,*], Shunlin Liang[b], Lian He[a], Chao Zeng[a], Xiaohua Hao[c], Yang Hong[a]

[a] State Key Laboratory of Hydroscience and Engineering, Department of Hydraulic Engineering, Tsinghua University, Beijing 100084, China
[b] Department of Geographical Sciences, University of Maryland, College Park 20740, USA
[c] Northwest Institute of Eco-Environmental and Resources, Chinese Academy of Sciences, Lanzhou 730000, China

ARTICLE INFO

Keywords:
Tibetan Plateau
Snow cover extent
AVHRR surface reflectance CDR
Climate change

ABSTRACT

Snow cover condition across the Tibetan Plateau (TP) is not only a significant indicator of climate change but also a vital variable in water availability because of its water storage function in high-mountain regions of Southwest China and the surrounding Asian countries. Limited by low spatial resolution, incomplete spatial coverage, and short time span of the current snow cover products, the long-term snow cover change across the TP under the climate change background remains unclear. To resolve this issue, a composite long-term gap-filled TP daily 5-km snow cover extent (SCE) record (TPSCE) is generated by integrating SCE from the Advanced Very High-Resolution Radiometer (AVHRR) surface reflectance climate data record (CDR) and several existing snow cover data sets, with the help of a decision tree snow cover mapping algorithm, for the period 1981–2016. A snow discrimination process was used to classify the land surface into snow (pre-TPSCE) and non-snow using AVHRR surface reflectance CDR. To fill gaps caused by invalid observations and cloud contamination in pre-TPSCE, several existing daily SCE products, including MOD10C1, MYD10C1, IMS, JASMES, and a passive microwave snow depth data set are employed in the composition process. The daily snow discrimination accuracy, tested by ground snow-depth observations during 2000–2014, shows that the TPSCE captures the distribution of snow duration days (R^2 = 0.80, bias = 3.93 days) effectively. The comparison between the TPSCE and fine-resolution snow cover maps (MCD10A1-TP) indicates high comparability between the TPSCE and MCD10A1-TP. In addition, cross-comparisons with changes in temperature, precipitation, and land surface albedo indicate that the TPSCE is reliable in climate change studies. In summary, the TPSCE is spatially complete and covers the longest period among all current snow cover products from satellite observations. The TPSCE seamlessly records changes in snow cover across the TP over the past 36 years, thereby providing valuable snow information for climate change and hydrological studies.

1. Introduction

Snow cover is a critical component of the cryosphere and climate system on both the local and the global scales. As the “third pole” and “Asian water tower” with the highest mid-latitude mountains and largest cryosphere extent outside the polar regions, the Tibetan Plateau (TP) largely affects the regional environment and controls climatic and environmental changes in China, Asia, and even the Northern Hemisphere (NH) at large (Kang et al., 2010; Larson, 2011; Ma et al., 2009; Pu et al., 2008; Yao et al., 2012). Snow cover on the TP has large potential to influence the regional hydrological cycle (Qian et al., 2011), affects the frequency of heat waves in northern China (Wu et al., 2012), and results in anomalies in vegetation greenness onset (Dong et al., 2013), the atmosphere–land interaction (Ma et al., 2009), and the East Asian summer monsoon (Pu et al., 2008). Furthermore, seasonal snow cover across the TP constitutes a vital source of surface water for Southwest China and the surrounding Asian countries (e.g., Pakistan, India, Nepal, Bangladesh, and Bhutan). Thus, quantifying snow cover conditions across the TP is essential for meteorological, hydrological, ecological, and societal implications.

Satellite remote sensing has been employed to map and monitor snow cover for more than forty years (Brown et al., 2010; Frei et al., 2012), because data collection by traditional field snow surveying is time consuming, costly, and extremely difficult. Using data sets, such as the binary daily snow cover mask derived from the Interactive Multisensor Snow and Ice Mapping System (IMS) (Helfrich et al., 2007), the Northern Hemisphere Weekly Snow Cover and Sea Ice Extent (NHSCE) (Helfrich et al., 2007; Robinson et al., 1993), the Moderate-Resolution

* Corresponding author.
E-mail address: dlong@tsinghua.edu.cn (D. Long).

https://doi.org/10.1016/j.rse.2018.06.021
Received 21 October 2017; Received in revised form 10 June 2018; Accepted 16 June 2018
Available online 26 June 2018
0034-4257/ © 2018 Elsevier Inc. All rights reserved.

Imaging Spectroradiometer (MODIS) snow cover products (Hall et al., 1995), the Suomi National Polar-orbiting Partnership (NPP) snow cover suite (Key et al., 2013), the European Space Agency (ESA) Global Snow Monitoring for Climate Research (GlobSnow) (Pulliainen, 2010), and snow water equivalent (SWE) products from the Advanced Microwave Scanning Radiometer-Earth Observing System (AMSR-E) (Kelly et al., 2003) and GlobSnow, the continental-scale snow cover anomalies are well quantified. Nevertheless, owing to complex topography, heterogeneous land cover types, and scattered snow cover distributions over the TP, as well as the limitations of the current snow cover data sets, the long-term snow cover condition across the TP remains unclear. Among the current snow cover products, the Suomi-NPP has high snow classification accuracy (> 90%) (Key et al., 2013), the MODIS snow cover products provide moderate spatial resolution (500 m) and high temporal resolution (Hall et al., 1995), the IMS provides complete spatial coverage (Helfrich et al., 2007), and the NHSCE provides the longest time span (4 October 1966 to the present) (Helfrich et al., 2007; Robinson et al., 1993). However, incomplete spatial coverage (e.g., Suomi-NPP and MODIS), short time span (e.g., Suomi-NPP and IMS), and low spatial resolution (e.g., NHSCE and GlobSnow) largely restrict the application of these products in snow cover studies across the TP.

To improve the understanding of snow cover changes over the TP under the climate change background, a long-term series, temporally consistent, and high-quality composite snow cover data set is needed. Accordingly, the objective of this study was to develop a composite long-term TP daily 5-km snow cover extent (SCE) record (TPSCE). To generate the preliminary daily TPSCE (pre-TPSCE) at the highest achievable spatial resolution and longest time span, we employed the newly published National Oceanic and Atmospheric Administration (NOAA) Advanced Very High-Resolution Radiometer (AVHRR) surface reflectance Climate Data Record (CDR) (Vermote et al., 2014) as primary data. To overcome the shortage of optical AVHRR images in snow discrimination (mainly caused by invalid observations and cloud contamination), several ancillary data sets were jointly used in this study. Moreover, to test the reliability of the TPSCE in climate change studies, temperature, precipitation, and land surface albedo data were employed for cross-comparison purposes.

This study comprises six sections. Section 2 describes the data sets used in the study. Section 3 presents the processing flowchart for the TPSCE. In Section 4, we compare the TPSCE with ground snow-depth observations and fine-resolution snow cover maps. We analyze the spatiotemporal variability in SCE from the TPSCE in Section 5 and present cross-comparisons with temperatures, precipitation, and land surface albedo. Finally, in Section 6, we summarize this study and present our conclusions.

2. Data sets and methodology

2.1. Data sets

2.1.1. AVHRR surface reflectance CDR

The AVHRR surface reflectance CDR is processed from the AVHRR Global Area Coverage (GAC) Level 1b data set. The AVHRR GAC observations are packaged into data arrays, with latitudinal and longitudinal dimensions of 3600 × 7200, covering the globe at 0.05° spatial resolution (Vermote et al., 2014). The spectral bands of AVHRR surface reflectance CDR are summarized in Table 1. The quality control descriptions are listed in Table 2.

Compared with AVHRR data sets used in previous studies (Hori et al., 2017; Zhou et al., 2013), AVHRR surface reflectance CDR provides consistent daily average surface reflectance and brightness temperatures that are derived from the AVHRR sensors onboard seven NOAA polar orbiting satellites, including NOAA-7, NOAA-9, NOAA-11, NOAA-14, NOAA-16, NOAA-17, and NOAA-18 (Vermote et al., 2014). Moreover, AVHRR surface reflectance CDR calibrates different instruments from 1981 to the present and facilitates their use in current snow mapping studies. Evaluating the AVHRR surface reflectance CDR performance by cross-comparison with MODIS in the monitoring of United States wheat yield demonstrated that the utility errors of AVHRR surface reflectance CDR were equivalent to those derived from MODIS (Franch et al., 2017). Therefore, this AVHRR historical data set was found to be reliable in land cover classification, especially for years before 2000. In addition, to reduce the snow discrimination error caused by distortions in pixel geometry, only images with a view zenith angle of < 45° were used in this study.

Compared with binary snow cover products, fractional snow cover products would provide better accuracy because of fragmented snow distributions in the TP. However, due to complex topography and relatively low spatial resolution of AVHRR surface reflectance CDR (0.05°), the selection of end-members within a grid cell across the TP is variable and uncertain, which limits the application of spectral unmixing algorithms among images with different times and locations. Thus, we developed binary snow products instead of fractional snow cover products in this study.

Table 1
Details of spectral bands of AVHRR surface reflectance CDR used in this study.

Bands	Wavelength (mu)	Description
1	0.58–0.68	Surface reflectance at 640 nm (SR1)
2	0.725–1.00	Surface reflectance at 860 nm (SR2)
3	3.55–3.93	Surface reflectance at 3.75 μm (SR3)
4	3.55–3.93	Brightness temperature at 3.75 μm (BT37)
5	10.30–11.30	Brightness temperature at 11.0 μm (BT11)
6	11.50–12.50	Brightness temperature at 12.0 μm (BT12)
7	–	Quality control flag

Table 2
Quality control descriptions of AVHRR surface reflectance CDR used in this study.

Bit	Description	Value = 1	Value = 0
15	Polar flag (latitude over 60 degrees (land) or 50 degrees (ocean))	Yes	No
14	BRDF-correction issues	Yes	No
13	RHO3 value is invalid	Yes	No
12	Channel 5 value is invalid	Yes	No
11	Channel 4 value is invalid	Yes	No
10	Channel 3 value is invalid	Yes	No
9	Channel 2 value is invalid	Yes	No
8	Channel 1 value is invalid	Yes	No
7	Channels 1–5 are valid	Yes	No
6	Pixel is at night (high solar zenith)	Yes	No
5	Pixel is over dense dark vegetation	Yes	No
4	Pixel is over sunglint	Yes	No
3	Pixel is over water	Yes	No
2	Pixel contains cloud shadow	Yes	No
1	Pixel is cloudy	Yes	No

2.1.2. Ancillary data

2.1.2.1. MODIS daily snow cover products. The MODIS Terra/Aqua Snow Cover Daily L3 Global 0.05° Climate Modeling Grid (CMG) (MO/YD10C1) (Hall et al., 1995) reports the percentage of snow-covered land at 0.05° spatial resolution for the period 2000 to the present and 2002 to the present, respectively. The percentages are computed from snow cover observations in the MODIS Terra/Aqua Snow Cover Daily L3 Global 500-m Grid (MO/YD10A1) data set (Hall et al., 1995). The overall absolute accuracy of MOD10A1 is higher than 93% under ideal conditions of illumination, clear skies, and several centimeters of snow on a smooth surface (Hall and Riggs, 2007). A study by Polashenski et al. (2015) indicated that Collection 5 MODIS data, particularly that of Terra, showed systematic temporal trends in visible and near-infrared bands. To avoid uncertainties induced by this issue in MO/YD10C1, we used collection 6 MO/YD10C1 in our study.

However, limited by cloud contamination, swath coverage, warm bright surface features, and low illumination, the spatial coverages of MO/YD10C1are not complete.

2.1.2.2. IMS snow cover product. The IMS snow cover product is created manually by a snow analyst observing all the available satellite imagery, automated snow mapping algorithms, and other ancillary data (Helfrich et al., 2007). This data set provides daily snow cover maps for the NH from February 1997 to the present at three different resolutions, i.e., 1 km, 4 km, and 24 km. To fill the gaps in the pre-TPSCE at the highest achievable spatial resolution, we used the IMS snow mask at 4-km spatial resolution from early 2004 to the present. The daily rate of agreement between the IMS snow maps and ground snow observations between 2006 and 2010 ranged mostly between 80% and 90% through winter seasons (Chen et al., 2012). However, the snow classification accuracy of IMS is only 60% because of serious omission error over the TP as was evaluated by Yu et al. (2016).

2.1.2.3. JASMES snow cover product. The NH daily 5-km SCE product (JASMES) was developed by the application of a consistent objective snow cover mapping algorithm to data from historical optical sensors on polar orbiting satellites during 1978–2015, including AVHRR GAC radiance data of NOAA from November 1978 to December 2005, and MODIS radiance data (MOD02SSH of Terra, MYS02SSH of Aqua) from March 2000 to December 2015 (Hori et al., 2017). Owing to gaps caused by track, swath, solar zenith angle, view zenith angle, and cloud contamination, the JASMES daily SCE data are not spatially complete. Comparison with NOAA weekly SCE that is corrected by in situ data indicates the reliability of the long-term trends of the JASMES product. However, the correlation between the annual snow duration (SCD) trends derived from both in situ measurements and JASMES showed that there is not only a weak correlation between SCD trends from the JASMES and in situ data ($R = 0.330$ for NH) but also an overestimation tendency of the JASMES-derived trends (Hori et al., 2017). Since the systematical error between AVHRR and MODIS could influence the consistency of the JASMES data set, we used only the JASMES generated by the NOAA AVHRR GAC radiance data in this study.

2.1.2.4. Passive microwave snow-depth data. Compared with optical remote sensing, passive microwave sensors offer the potential to estimate snow cover under cloudy conditions (Frei et al., 2012). To partially address the cloud contamination issue that exists in optical snow cover data sets, the passive microwave derived snow-depth data set (PSD) developed by Che et al. (2008) was employed in this study. The PSD data set at 25-km spatial resolution was retrieved from inter-calibrated brightness temperature data from the Nimbus-7 Scanning Multichannel Microwave Radiometer (SMMR) during 1978–1987, the Defense Meteorological Satellite Program (DMSP) Special Sensor Microwave/Imagers (SSM/I) during 1987–2007, and the DMSP Special Sensor Microwave Imager/Sounder (SSMI/S) during 2008–2016 by using the modified Chang algorithm and a dynamically adjusted algorithm (Che et al., 2008). The inter-sensor calibration improved the consistency of the daily snow-depth products and provided a temporally consistent, long-term series of snow-depth data set over China, which were important in the development of the TPSCE. However, there are misclassification and errors in the PSD-derived SCE due to relatively coarse spatial resolution of passive microwave remote sensing, ground temperature, snow characteristics and topography according to Dai et al. (2017), especially over the frozen ground (Tsutsui and Koike, 2012).

2.1.2.5. Landsat 5 TM data. Landsat 5 TM images at 30-m spatial resolution were employed as “ground truth” to adjust the threshold of the normalized difference snow index (NDSI) applied in the snow discrimination process. Since both Landsat 5 TM images and AVHRR surface reflectance CDR are often contaminated by cloud cover, few images are ideal in the comparison process. After cross-comparison of cloud cover from Landsat 5 TM images and AVHRR surface reflectance CDR, only two Landsat 5 TM images were selected in this study. Details of the two Landsat 5 images are listed in Table 3.

Table 3
Details of Landsat images used in this study.

No.	Path	Row	Date	Cloud cover (%)	Latitude (°N)	Longitude (°N)
A	149	035	2011-04-27	2.85	75.23	36.05
B	151	035	2011-04-25	1.86	72.15	36.05

2.1.2.6. Land cover types data. To increase the snow discrimination accuracy from the AVHRR surface reflectance CDR, the generation of the TPSCE was initiated within the framework of the International Geosphere Biosphere Program (IGBP) land cover types from MCD12Q1. The IGBP divides the land surface into 17 types, including 11 natural vegetation types, 3 land use and land mosaic types, and 3 vegetation-free land types (Friedl et al., 2010). The land cover types over the TP derived from MCD12Q1 in 2012 are presented in Fig. 1.

To increase the effectiveness of discriminating snow cover from other land surfaces, we re-classified the land cover types defined by the IGBP across the TP into four types, i.e., (1) mixed forest and shrublands, (2) grasslands, (3) barren land, and (4) snow and ice. The mixed forest and shrublands, including evergreen needle-leaf forest, evergreen broad-leaf forest, mixed forest, closed shrublands, open shrublands, and woody savannas are defined by the IGBP. The grasslands, including cropland/natural vegetation, grasslands, and cropland are also defined by the IGBP. The barren land, including barren or sparsely vegetated, urban, and built-up is defined by the IGBP. The snow and ice types equal to the types defined by the IGBP.

2.1.2.7. Elevation data. To detect cloud before the snow discrimination process, the digital elevation model (DEM) derived from the Shuttle Radar Topography Mission (SRTM) was used in this study. To match the resolution of the AVHRR surface reflectance CDR, we resampled the original SRTM DEM data at a 90-m resolution to a 0.05° spatial resolution by using a resampling method of ″average″ with the help of gdalwarp (http://www.gdal.org/gdalwarp.html).

2.1.3. Cross-comparison data

2.1.3.1. Ground snow-depth observations. The ground snow-depth observations were needed to verify the performance of the TPSCE to capture the actual snow distribution across the TP. In this study, daily snow-depth observations for the period 2000–2014 were employed for this purpose. The daily snow-depth observations were obtained from the Data Sharing Service Platform of the China Meteorological Administration (CMA, http://data.cma.cn/). The distribution of 72 ground snow-depth observations employed in this study is shown in Fig. 2.

2.1.3.2. MCD10A1-TP snow cover products. The combined fine-resolution cloud-free gap-filled MODIS daily snow cover data set across the TP (MCD10A1-TP) developed by Huang et al. (2014) was used in this study to compare with the climatology and anomalies of the snow cover over the TP calculated from the TPSCE. MCD10A1-TP was generated by using daily MOD10A1, MYD10A1, and AMSR-E SWE products. By combining optical and passive microwave snow products, the overall classification accuracy of MCD10A1-TP reaches 91.7% when the snow depth is > 3 cm (Huang et al., 2014), suggesting that MCD10A1-TP is suited for use as a benchmark in our study.

2.1.3.3. Land surface temperature data. To evaluate long-term snow

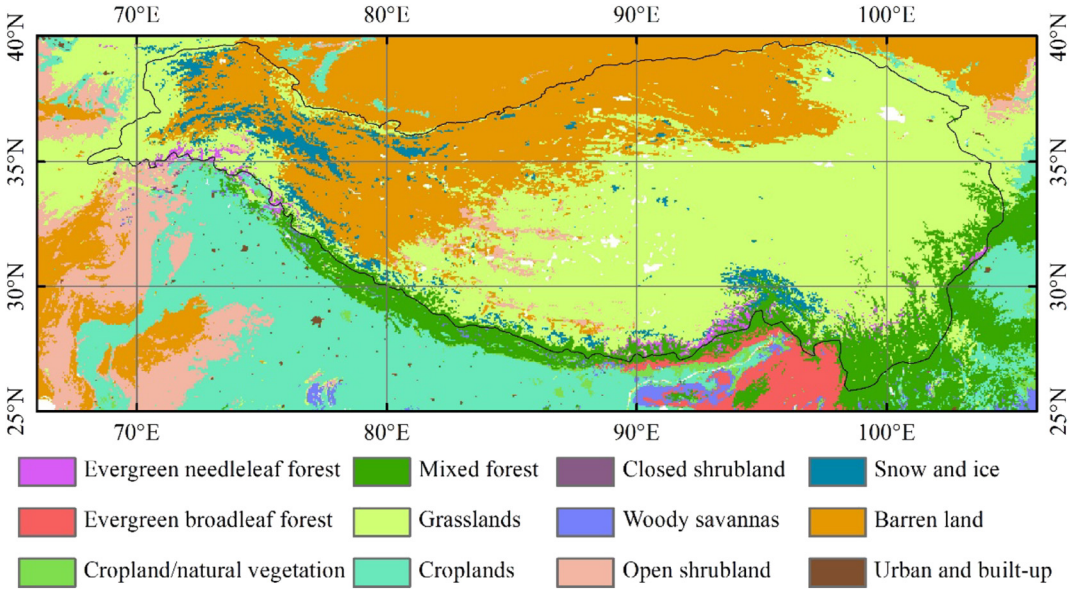

Fig. 1. Location and distribution of IGBP land cover types across the TP derived from MCD12Q1 in 2012.

cover changes derived from the TPSCE by cross-comparison, the daily-averaged land surface temperature data set, gridded at 0.25° horizontal resolution, derived from the European Centre for Medium-Range Weather Forecasts Reanalysis (ECMWF) (ERA-Interim) (Dee et al., 2011) during 1981–2016, was used in this study. ERA-Interim is widely employed in global and regional climate change studies, e.g., Chen et al. (2015), Cohen et al. (2010), and Cohen et al. (2014). Evaluation of ERA-interim monthly temperature data over the TP using 75 ground meteorological stations showed high correlations ranging from 0.97 to 0.99 during 1979–2010 (Gao et al., 2014).

2.1.3.4. Precipitation data. Similar with the land surface temperature data, the Precipitation Estimation from Remotely Sensed Information using Artificial Neural Networks-Climate Data Record (PERSIANN-CDR) (Ashouri et al., 2015) was also employed to compare with long-term snow cover changes derived from the TPSCE. PERSIANN precipitation CDR provides daily precipitation estimates at a spatial resolution of 0.25° in latitudes from 60°S to 60°N from 1983 to the end of 2015. This product was developed by using Gridded Satellite (GridSat-B1) infrared data that were derived from merging International Satellite Cloud Climatology Project (ISCCP) B1 infrared data and Global Precipitation Climatology Project (GPCP) version 2.2 (Ashouri et al., 2015).

2.1.3.5. CLARA-SAL land surface albedo data. Changes in snow cover have been shown to be related closely with anomalies in land surface albedo because of high reflectance of snow cover (Chen et al., 2015; Qu and Hall, 2014). Therefore, the long-term surface albedo data set derived from CLoud, Albedo and surface RAdiation data set from AVHRR data Edition 2 (CLARA-A2) during 1979 to 2015 at a spatial resolution of 0.25° was used to compare with the spatiotemporal variability in snow cover calculated from the TPSCE in our study. The CLARA-SAL surface albedo data set is generated based on a homogenized AVHRR radiance time series and is created by using algorithms to derive surface albedo for different land use areas separately, including snow, sea ice, open water, and vegetation. Currently, the CLARA-SAL surface albedo data set is the only available long time-span albedo product derived from AVHRR imagery (Riihelä et al., 2013).

2.1.4. Grid cell definition

A summary of data sets used in this study is listed in Table 4.

To match the spatial resolution of the AVHRR surface reflectance CDR, other data sets were regridded at a spatial resolution of 0.05° and an array resolution of 800 × 300 pixels with geographic latitude/longitude projection by using the resampling method of “average” or “cubic-spline” with the help of gdalwarp (http://www.gdal.org/

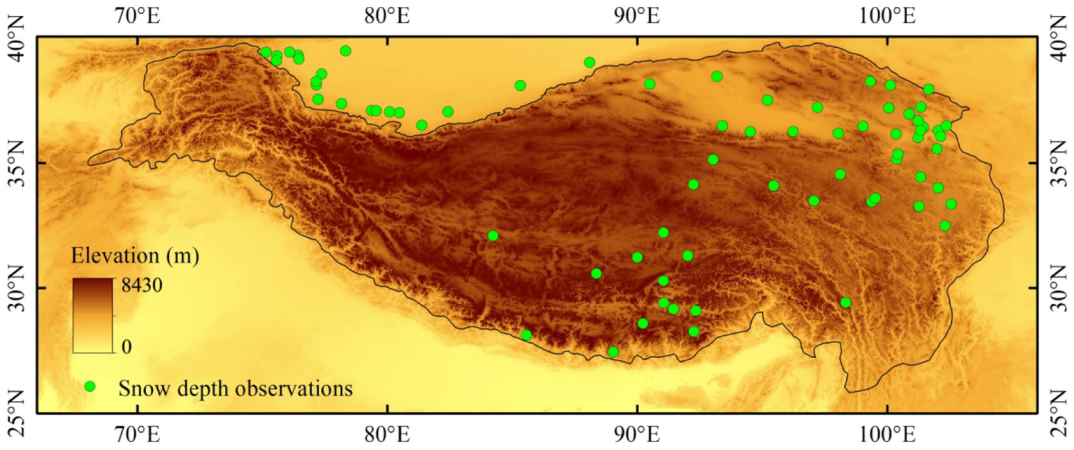

Fig. 2. Distribution of 72 ground snow-depth observations over the TP and surroundings for the period 2000–2014.

Table 4
Summary of data sets used in this study.

Data purpose	Datasets	Time span	Spatial resolution	Temporal resolution	References
Primary data	AVHRR surface reflectance CDR	1981–present	0.05°	Daily	Vermote et al. (2014)
Ancillary data	MOD10C1	2000–present	0.05°	Daily	Hall et al. (1995)
	MYD10C1	2002–present	0.05°	Daily	Hall et al. (1995)
	IMS	2004–present	4-km	Daily	Helfrich et al. (2007)
	JASMES	1978–2015	5-km	Daily	Hori et al. (2017)
	PSD	1978–2016	25-km	Daily	Che et al. (2008)
	ERA	1972–present	0.125°	Daily	Dee et al. (2011)
	SRTM DEM	–	90-m	–	http://seamless.usgs.gov/
	MCD12Q1	2012	0.05°	Yearly	Friedl et al. (2010)
Cross-comparison data	MCD10A1-TP	2000–2014	500-m	Daily	Huang et al. (2014)
	NHSCE	1966–2015	24-km	Weekly	Robinson et al. (1993)
	CLARA-A2	1979–2015	0.25°	Monthly	Riihelä et al. (2013)
	PERSIANN	1983–2015	0.25°	Daily	Ashouri et al. (2015)

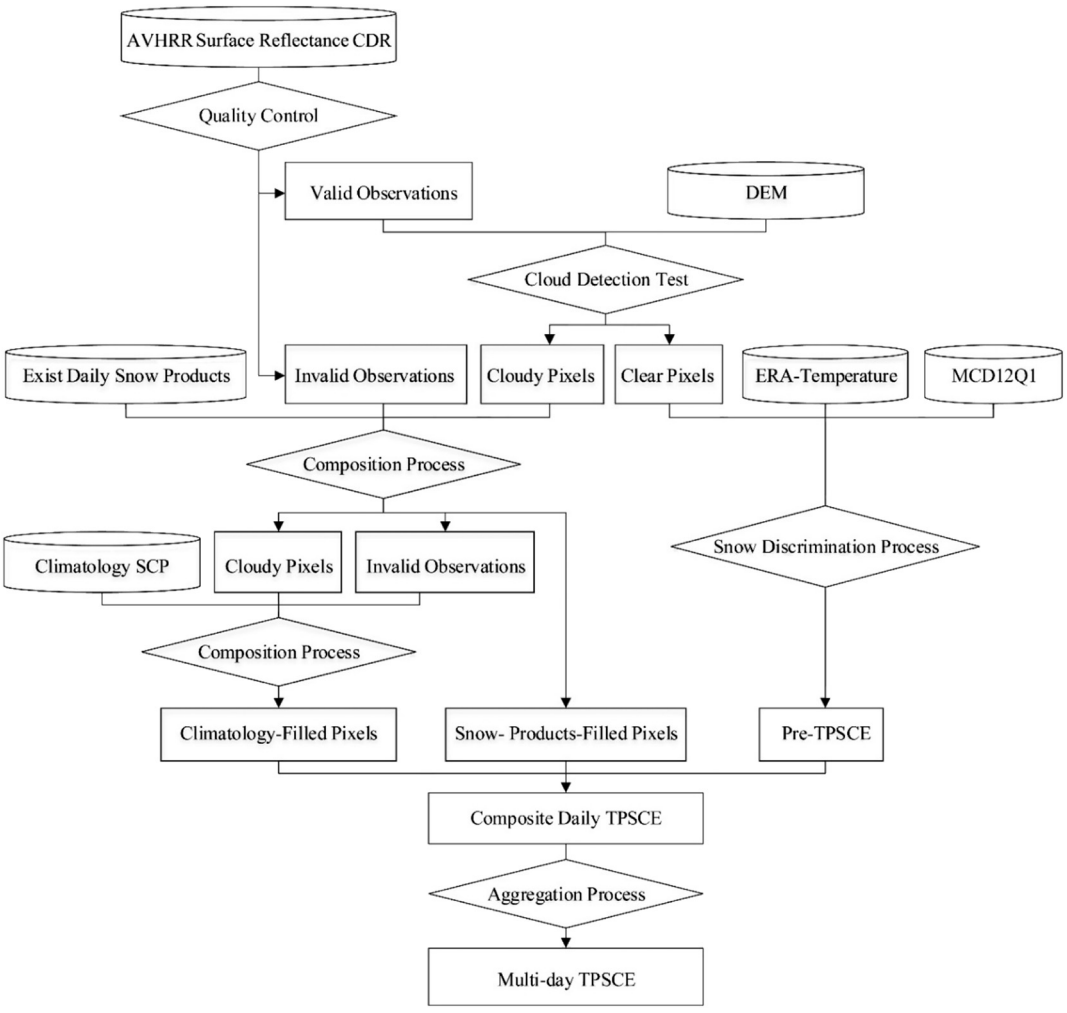

Fig. 3. Flowchart of TPSCE generation in this study.

gdalwarp.html). For data sets with a spatial resolution > 0.05°, we used "average" in the resampling process, which computed the average of all non-NODATA contributing pixels in the domain of our study. For data sets with a spatial resolution lower than 0.05°, we used "cubic-spline" in the resampling process. The latitude and longitude of the center of the upper left grid cell were set at 40.0°N and 66.0°E according to the location of TP, as shown in Fig. 1. The latitude and longitude data correspond to a center pixel of a 0.05° by 0.05° block of grid cells in the TPSCE.

2.2. Snow discrimination accuracy evaluation

2.2.1. Evaluation by ground snow-depth observations

Validating moderate-resolution satellite images by field measurements is difficult because a single grid cell from satellite measurements can measure the information from an extremely large area, which may overestimate or underestimate the information from a field measurement. However, the field measurements are still the most convincing records to test the reliability of satellite retrieved products. To estimate the snow discrimination accuracy of the TPSCE, we used snow duration

Table 5
Cloud detection tests and their threshold values.

Target	Switch	Height (m)	SR1 (−)	SR2 (−)	SR3 (−)	SR1–SR2 (−)	NDVI (−)	NDSI (−)	BT11 (K)	BT37-BT11 (K)	BT11-BT12 (K)
A	On	< 3000							≥240	> 8	
	On	≥3000							≥240	> 15	
B	On								< 240	> 20	
	On				> 0.1	> −0.02		< 0.88			
	Off						> 0.5		> 288		
	0ff								> 310		
	On								< 260	> 8	
	On					> −0.02			< 310	> 10	
	On		> 0.3			> −0.02			< 293	> 9	
	On			> 0.4		> −0.03			< 293	> 8	> −1
	On			> 0.4					< 278	> 20	> −1
	On		> 0.3		> 0.2				< 263		
	Off						> 0.5		> 288		
	Off								> 310		
	Off	> 1000	< 0.4			< −0.04			> 275		
	Off					< −0.05			> 300		

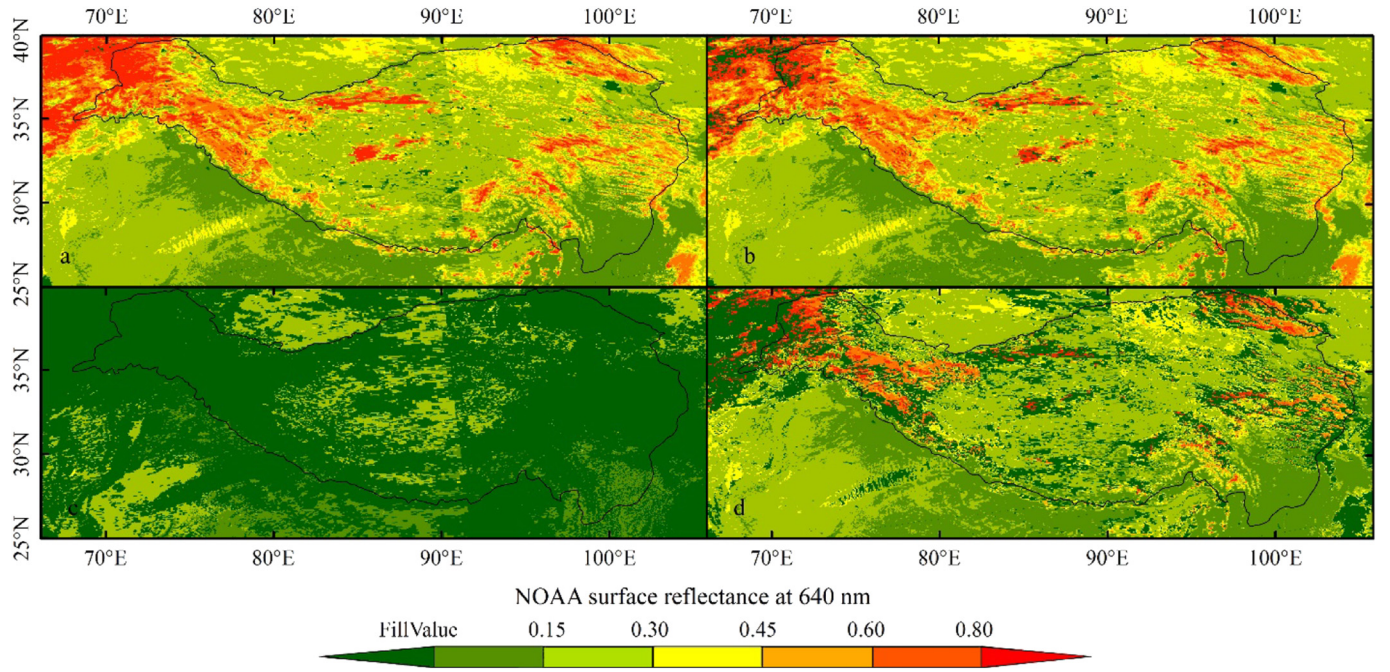

Fig. 4. (a) Raw AVHRR surface reflectance at 640 nm (SR1), (b) quality controlled SR1 (observations are valid), (c) cloud masked SR1 using cloudy flag, and (d) cloud masked SR1 using the cloud detection algorithm over the study area on December 31, 1981.

days (D_d) as criteria in comparison with ground snow depth observations (Fig. 2). For a given grid cell, D_d was defined as the number of days in a calendar year with snow cover on the ground.

2.2.2. Evaluation by fine-resolution MCD10A1-TP products

In addition to comparisons with ground snow-depth observations, comparison with higher spatial-resolution images is widely used in the validation of moderate-resolution satellite images, such as by Hall et al. (1995). Compared with the newly developed TPSCE, the MCD10A1-TP represents consistent and objective snow estimates derived from high-resolution optical remote sensing data. Therefore, the MCD10A1-TP was used as the benchmark for the TPSCE. The root-mean-square error (RMSE) and bias were used as criteria to evaluate the relative accuracy of the TPSCE relative to MCD10A1-TP during the period 2001 to 2014. The RMSE and bias of the TPSCE to MCD10A1-TP are expressed as follows:

$$RMSE = \sqrt{\frac{1}{n}\sum_{i-1}^{n}(T_i - M_i)^2} \quad (1)$$

$$Bias = \frac{1}{n}\sum_{i=1}^{n}(T_i - M_i) \quad (2)$$

where M_i and T_i are the snow cover fraction (SCF) of sample i in the 500-m MCD10A1-TP and 5-km TPSCE snow cover products, respectively.

3. Processing flowchart of TPSCE

3.1. Flowchart of TPSCE generation

The flowchart of TPSCE generation is presented in Fig. 3. First, by using the quality control flag (Table 2), the grid cells with valid observations in channels 1–5 were employed in the pre-TPSCE generation, in which the quality control flags of "1" in bit 7, indicating channels 1–5

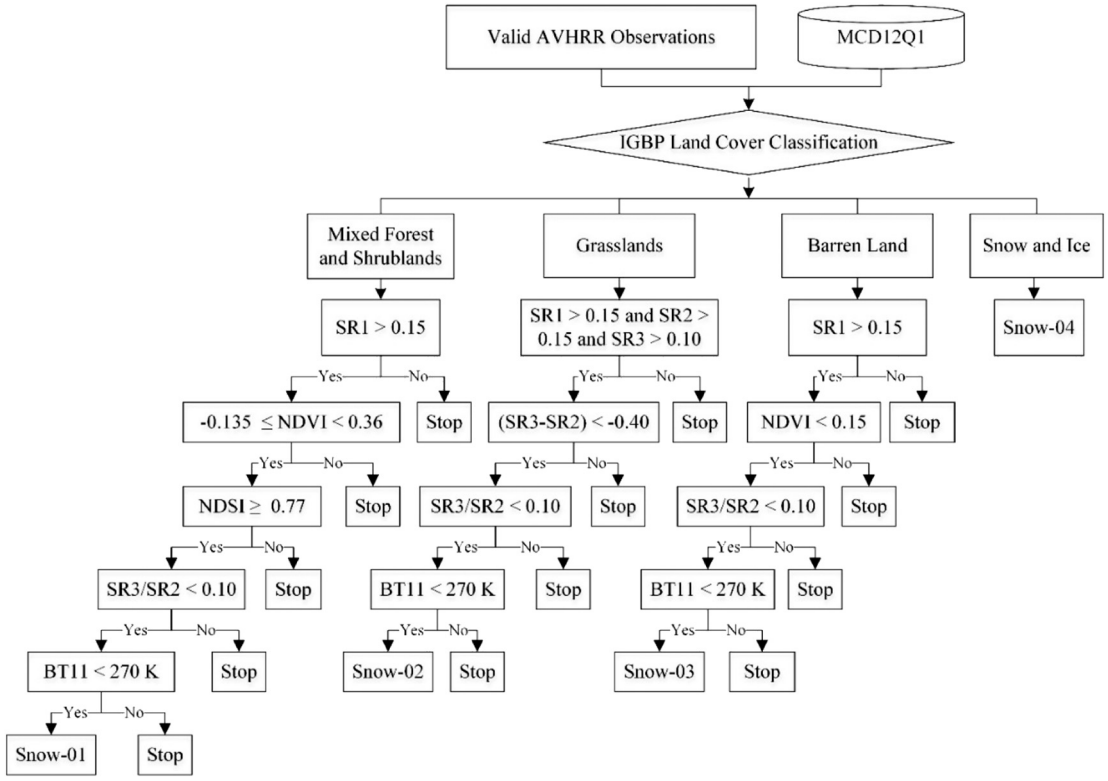

Fig. 5. Decision tree and threshold values for snow discrimination using AVHRR surface reflectance CDR.

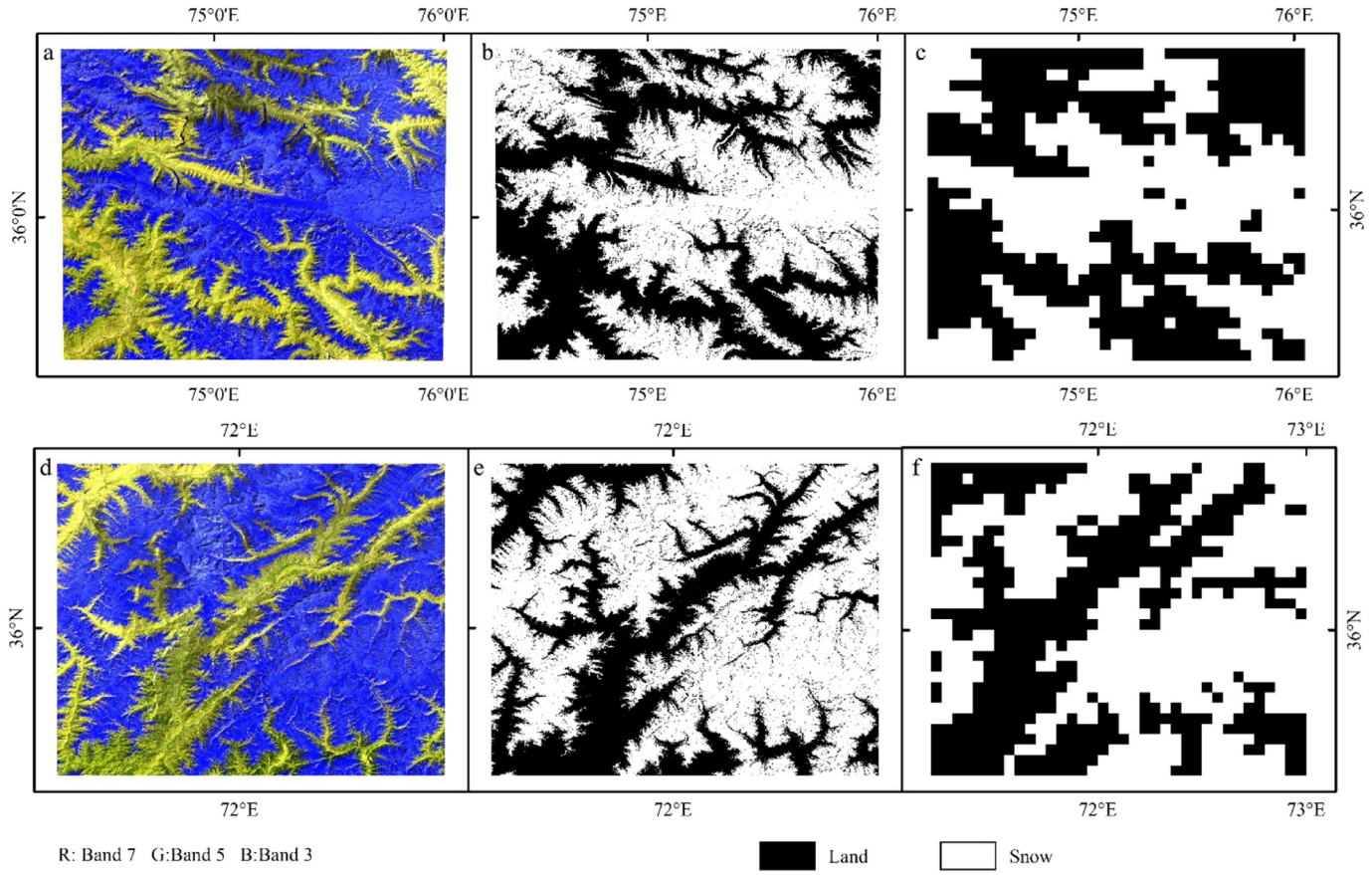

Fig. 6. False color images of (a) A and (d) B listed in Table 3. Snow cover extent retrieved by the SNOMAP algorithm of (b) A and (e) B. Snow cover extent retrieved by AVHRR surface reflectance CDR using an NDSI threshold of 0.80 of (c) A and (f) B. In the combination of Landsat 5 bands 7, 5, 3 as RGB, snow appears in blue on the landscape. (For interpretation of the references to color in this figure legend, the reader is referred to the web version of this article.)

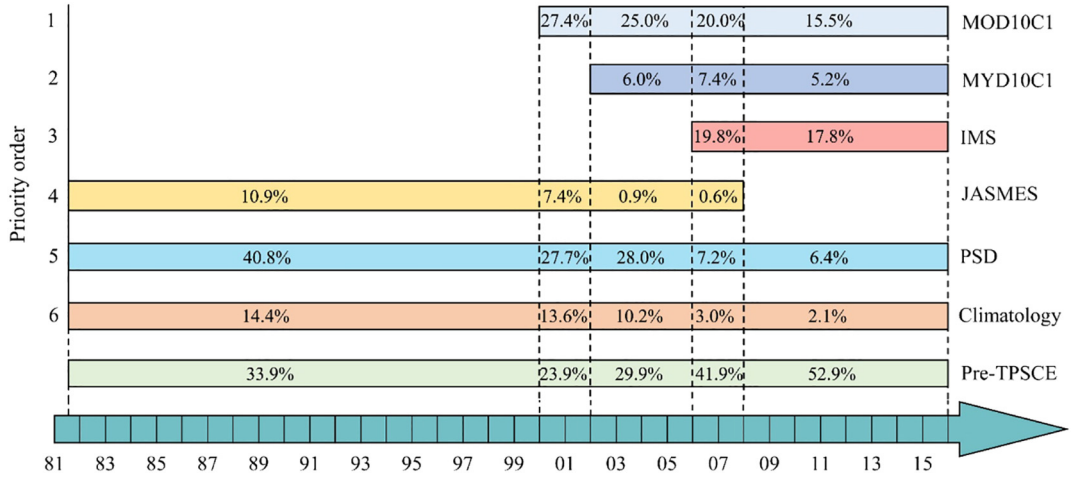

Fig. 7. Priority order of integrating existing snow cover products with the pre-TPSCE and their contributions to the composite TPSCE.

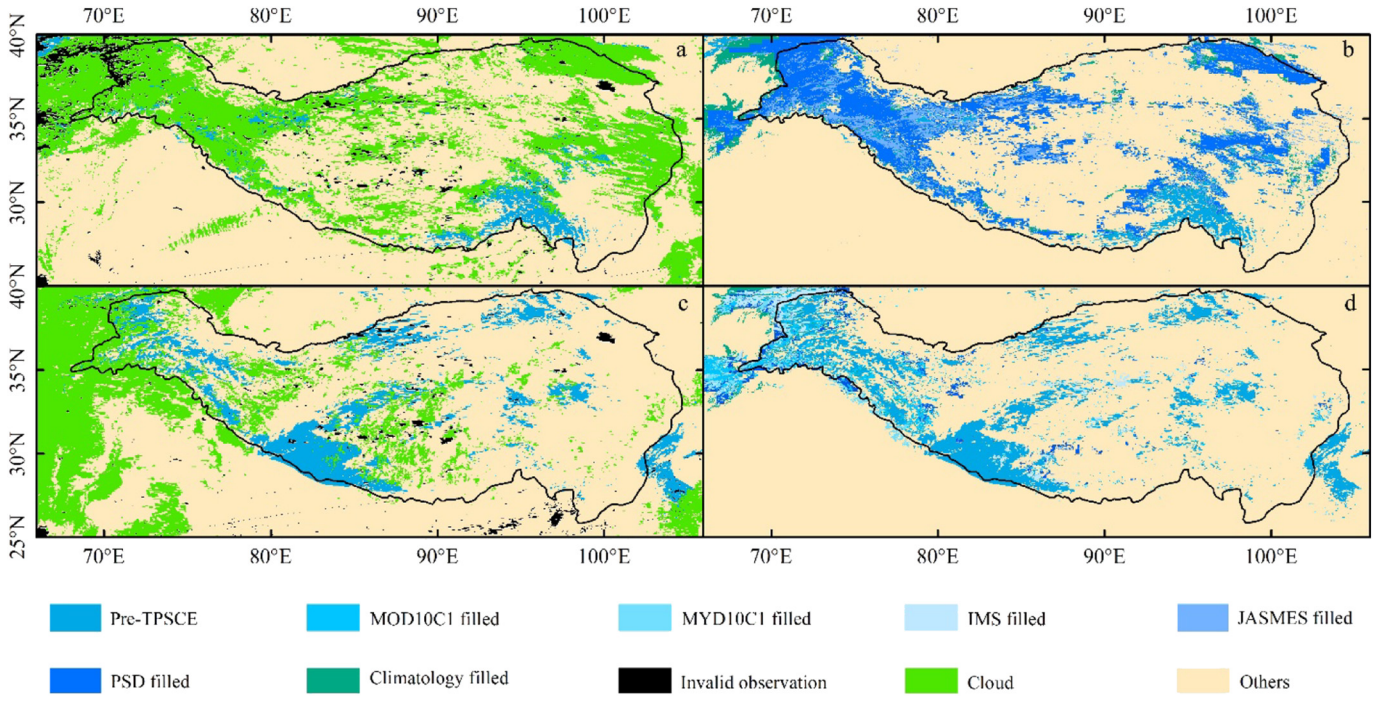

Fig. 8. Comparisons of (a and c) the pre-TPSCE and (b and d) TPSCE on December 31, 1981 and January 01, 2015 over the study area.

Table 6
Descriptions of composite daily TPSCE.

Value	Description	Value	Description
0	Non-snow	5	Pixel is filled by IMS
1	Pre-TPSCE	7	Pixel is filled by JASMES
2	Pixel is filled by MOD10C1	11	Pixel is filled by PSD
3	Pixel is filled by MYD10C1	13	Pixel is filled by Climatology

that are valid were selected. Second, the cloud detection test was conducted with the help of elevation to reduce the impacts of cloud in the snow discrimination process. The cloud detection test and their threshold values are listed in Table 5. The example of cloud detection test over the study area on December 31, 1981 is presented in Fig. 4. Third, the pre-TPSCE was retrieved from valid AVHRR surface reflectance observations through the snow discrimination process using the decision tree approach. The decision tree and threshold values for snow discrimination are summarized in Fig. 5. The adjustment of NDSI threshold in snow discrimination process is shown in Fig. 6. Fourth, the grid cells with invalid AVHRR surface reflectance observations and cloudy were filled by existing daily snow cover products (including MO/YD10C1, IMS, JASMES, and PSD) through the composition process according to the priority order shown in Fig. 7. Fifth, the invalid observations and cloudy pixels after the composition process were filled by the climatology of the snow cover conditions. Examples of pre-TPSCE and TPSCE over the study area on December 31, 1981 and January 01, 2015 are displayed in Fig. 8. Finally, the multi-day TPSCE was produced through aggregation of daily TPSCE.

3.2. Cloud detection test

We did not adopt the cloudy and cloud shadow flag that accompanies the AVHRR surface reflectance CDR. This is because the cloudy flag appears to overestimate cloudy pixels that exist in the AVHRR surface reflectance CDR compared with cloudy pixels retrieved from the cloud detection test used by Hori et al. (2017) and previous studies. To

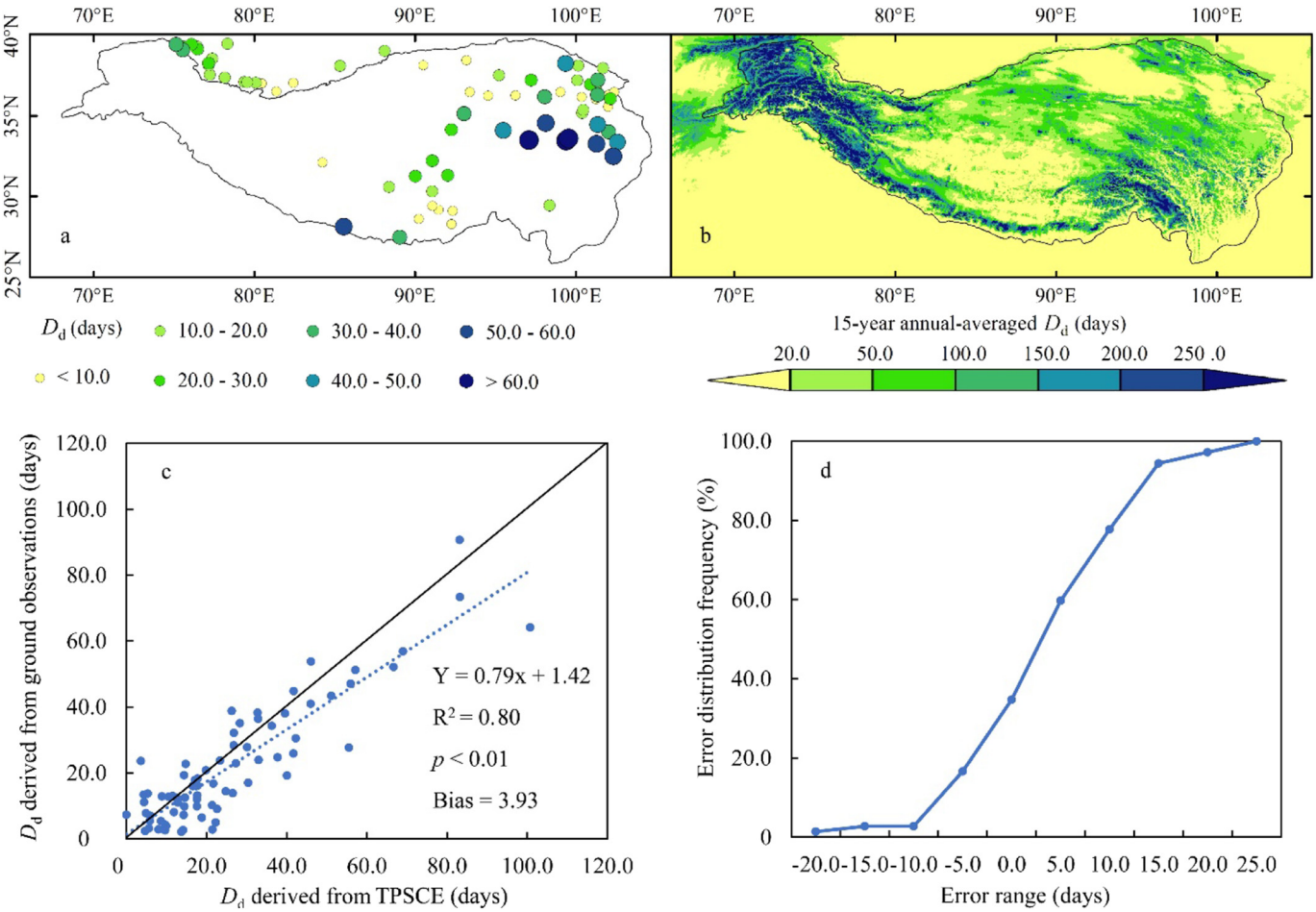

Fig. 9. Climatology of snow duration days D_d calculated from (a) 72 in situ snow-depth observations, and (b) the TPSCE across the TP for the period 2000–2014. (c) Comparisons between the climatology of D_d calculated from the TPSCE and in situ observations. (d) Error distribution frequency of D_d calculated from the TPSCE across the TP for the period 2000–2014.

resolve this issue, we employed the cloud detection test and threshold values according to Hori et al. (2017).

This table comes from Hori et al. (2017). Target A indicates high and cold land (elevation > 300 m and BT11 < 260 K); Target B indicates other land. The cloud detection test was conducted from the top of the list to the bottom for each target. If the cloudy flag switch was "on", the pixel was set to cloudy when the threshold tests met the conditions listed on the right-hand side. If the switch was "off", the pixel identified as cloudy in the previous tests was reset to clear. NDVI = (SR2-SR1)/(SR2 + SR1). NDSI = (SR1-SR3)/(SR1 + SR3).

Nine variables calculated from the AVHRR surface reflectance CDR (Table 1) were used in the cloud detection test, including SR1, SR2, SR3, BT11, differences between SR1 and SR2 (SR1-SR2), differences between BT37 and BT11 (BT37-BT11), differences between BT11 and BT12 (BT11-BT12), the normalized difference vegetation index (NDVI), and NDSI. The cloud detection tests and their threshold values are summarized in Table 5. The differences between the cloudy flag in AVHRR surface reflectance CDR and cloud detection test used by Hori et al. (2017) are shown in Fig. 4. Compared with cloud masked SR1 using cloudy flag (Fig. 4(c)), cloud masked SR1 using the cloud detection algorithm (Fig. 4(d)) provides more reasonable surface reflectance observations.

3.3. Snow discrimination process

A snow discrimination process was used to classify the land surface into snow and non-snow. According to the IGBP land cover classification (Fig. 1), grid cells were classified into four types at the start of the snow discrimination flow. The variables and thresholds for snow and non-snow discrimination adopted in the decision tree are shown in Fig. 5, in which the pre-TPSCE is defined as the combination of Snow-01 to Snow-04. Most of these threshold values in pre-TPSCE generation were not new but, rather, were combinations of the conventional snow detection tests employed in previous studies (Hori et al., 2017; Khlopenkov and Trishchenko, 2007; Kidder, 1987; Zhou et al., 2013).

As shown by published studies (Hall et al., 1995; Hall et al., 2002), the NDSI could distinguish effectively between snow and non-snow by referring to the NDVI, particularly in dense vegetation regions. In Hall et al. (1995), the NDSI was calculated by using the red (approximate wavelength of 630 nm) and shortwave infrared (1.64 μm) bands. As there are no shortwave infrared observations around the 1.64 μm wavelength in AVHRR surface reflectance CDR, we used the reflectance at 3.7 μm for an NDSI-like calculation, following Hori et al. (2017). Moreover, Hori et al. (2017) used 0.80 as the NDSI threshold to develop JASMES using AVHRR observations over the NH. Given the complex topography and unique snow properties in the TP, this NDSI threshold needs to be adjusted before used in the pre-TPSCE generation.

The comparisons between the SCE retrieved from Landsat 5 TM images and AVHRR surface reflectance CDR are shown in Fig. 6. The SNOMAP algorithm (Hall et al., 1995) was applied to retrieve SCE from Landsat 5 TM images. As presented in Fig. 6(b) and (d), SCE was well mapped by the SNOMAP algorithm compared to the false color images displayed in Fig. 6(a) and (c). The snow cover fraction (SCF) of A and B

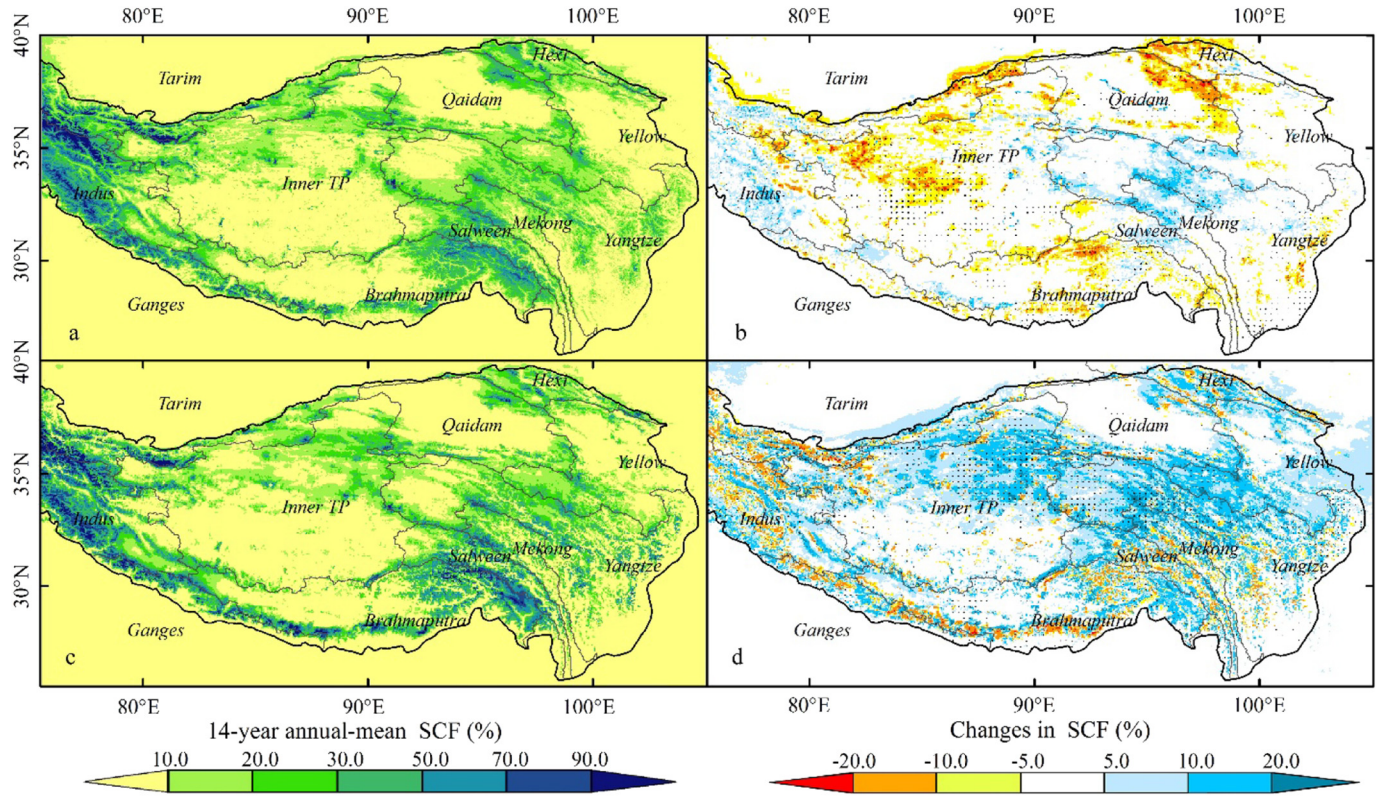

Fig. 10. Climatology of SCF (%) calculated from (a) MCD10A1-TP and (c) TPSCE for the period 2001–2014 across the TP and each basin for the period 2001–2014. Changes in SCF (%) were calculated from (b) MCD10A1-TP and (d) TPSCE across the TP and each basin for the period 2001–2014. Black spots in (b) and (d) indicate that the changes are statistically significant at the 95% level.

calculated from Landsat 5 TM images are 54% and 60%, respectively, whereas the SCF of A and B calculated from AVHRR surface reflectance CDR by using 0.80 as the NDSI threshold are 52% (Fig. 6e) and 56% (Fig. 6f). This means that using 0.80 as the NDSI threshold may underestimate SCE in the snow discrimination process. To resolve this issue, we adjusted the NDSI threshold from 0.80 to 0.77 by trial-and-error. In this case, the SCF of A and B calculated from AVHRR surface reflectance CDR was 55% and 61%, respectively, which are very similar to those fractions derived from Landsat 5 TM images.

3.4. Composition process

To improve the spatial coverage and reduce the omission error of the pre-TPSCE, a composition process was carried out to fill gaps caused by invalid observations and cloudy pixels. Several existing daily snow cover products were used in the composite procedure, including MO/YD10C1, IMS, JASMES, and PSD. The descriptions of the composite TPSCE are summarized in Table 6.

The priority order of integrating these snow cover products with the pre-TPSCE and their contributions in the daily TPSCE are presented in Fig. 7.

The priority order (Fig. 7) of integrating existing daily snow cover products with the pre-TPSCE was determined according to their spatial resolution. Compared with other ancillary snow cover data sets, both MOD10C1 and MYD10C1 represent consistent and objective snow estimates derived from high-resolution optical remote sensing data. Therefore, the MODIS snow cover data set was used as the first choice in gap filling for the pre-TPSCE. As the JASMES snow cover data set used both AVHRR and MODIS radiance data, which is repeated by the existing MODIS daily snow cover data set, we adopted only the JASMES data derived from AVHRR GAC radiance data during 1981–2008 in the composition process. In addition, to fill gaps induced by invalid observations and cloud contamination after the composite process, we calculated the climatology of daily snow cover probability for each grid cell by using IMS for the period 2005–2016. For a given grid cell, the snow cover probability in a given period was calculated by the number of years with snow cover divided by the number of years. For gaps that still exist after the composite process, the climatology of snow cover probability was employed to discriminate snow from non-snow areas. For grid cells with gaps, the snow cover probability > 50% was masked as snow. Examples of the pre-TPSCE and composite TPSCE on December 31, 1981 and January 01, 2015 are shown in Fig. 8.

3.5. Aggregation process

In order to compare the TPSCE with the current multi-day snow cover data sets, e.g., the 8-day MODIS snow cover data set, weekly NHSCE data set, 5-day AMSR-E SWE products, and other land surface variables, e.g., 5-day CLARA-SAL surface albedo products and 8-day MODIS leaf area index products, it was necessary to generate composite SCE data sets at varying temporal resolutions. For multi-day TPSCE, only grid cells with snow cover probability greater than or equal to 50% were defined as snow-covered regions.

4. Snow discrimination accuracy of the TPSCE

4.1. Comparisons with ground snow-depth observations

Subject to the data availability of CMA snow-depth observations, the comparison between the TPSCE and snow-depth observations was carried out during 2000–2014. The climatology of D_d, calculated from the TPSCE and 72 ground snow-depth observations across the TP for the period 2000–2014 is shown in Fig. 9.

Fig. 9(a) shows the spatial patterns of the 15-year climatology of D_d over the CMA-covered stations during 2000–2014. There are clear altitudinal gradient patterns for D_d from low to high altitudes. At most

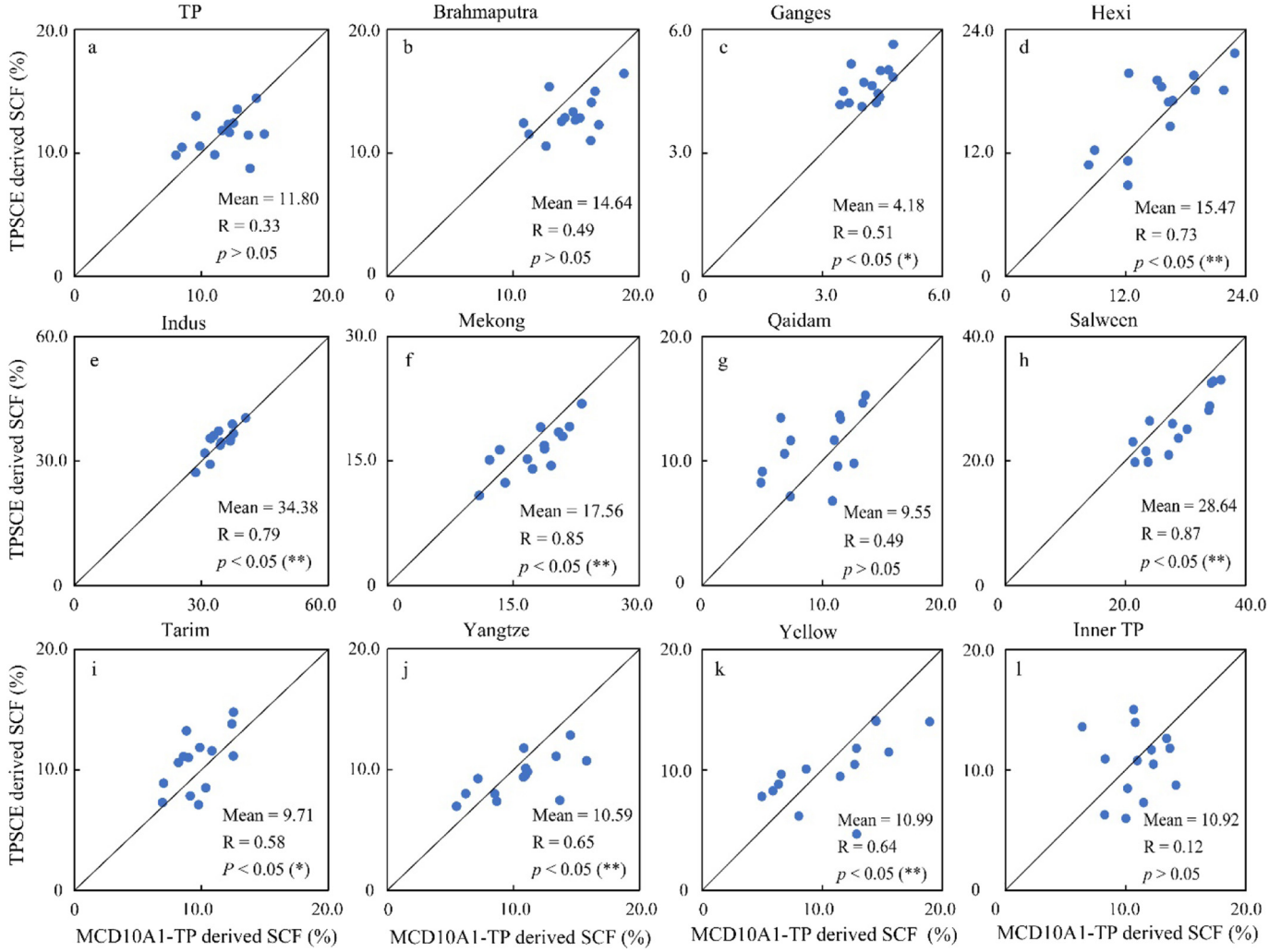

Fig. 11. Linear correlations between annual-mean SCF (%) calculated from MCD10A1-TP and TPSCE for the period 2001–2014 in (a) entire TP, (b) Brahmaputra, (c) Ganges, (d) Hexi, (e) Indus, (f) Mekong, (g) Qaidam, (h) Salween, (i) Tarim, (g) Yangtze, (k) Yellow, and (l) Inner TP. * indicates the linear correlation is significant at the 95% level, ** indicates the linear correlation is significant at the 99% level, whereas the others are not significant at the 95% level. (For interpretation of the references to color in this figure legend, the reader is referred to the web version of this article.)

Table 7
RMSE and bias for SCF (%) calculated from the TPSCE and MCD10A1-TP across the TP and each basin for the period 2001–2014.

Basin	RMSE (%)	Bias (%)	Basin	RMSE (%)	Bias (%)
TP	2.15	−0.25	Mekong	2.51	−1.26
Brahmaputra	2.53	−1.58	Qaidam	3.27	1.52
Ganges	0.64	0.47	Salween	3.79	−2.80
Hexi	3.04	0.71	Tarim	2.16	0.92
Yellow	3.31	−0.93	Inner TP	3.44	−0.37
Indus	2.14	0.40	Yangtze	2.56	−1.13

sites, the observed D_d is consistent with the TPSCE-retrieved D_d results (Fig. 9(b)), with an R^2 value of 0.80 at the 99% significant level. However, the bias in the TPSCE-retrieved D_d and the observed D_d is positive, with a value of 3.93 days (Fig. 9(c)), which means that the TPSCE tends to overestimate actual D_d across the TP during 2000–2014. Moreover, as shown in Fig. 9(c), TPSCE-retrieved D_d is higher than the ground observed D_d, particularly in the lower end of the D_d scale. These phenomena were caused mainly by the low spatial resolution of the TPSCE, which provide the averaged D_d value at the pixel scale. As the spatial resolution of the TPSCE is limited, the minima units in the TPSCE-retrieved D_d are pixels at 0.05°, which cannot catch and reflect entirely the actual (real) D_d at a specific spot location.

The error distribution frequency of the differences between the TPSCE-retrieved D_d and the in situ observed D_d (TPSCE-retrieved D_d minus in situ observed D_d) is shown in Fig. 9(d). The overestimated D_d accounts for 65.2% of the total 72 stations used in this study, in which 25% and 18% of the stations distributed an error range between 0 and 5 days and 5–10 days, respectively. Previous research has shown that the raw in situ observations would give results that depend highly on a particular location (latitude and elevation) (Hansen et al., 2010). Such results would reflect mostly those accidental snow circumstances, rather than yield meaningful climatology value of D_d. However, as shown in Fig. 9, D_d retrieved by the TPSCE still skillfully captures the D_d distributions over the TP. Although the TPSCE generally overestimates D_d across the TP, the bias (3.93 days) is still acceptable in snow phenology studies compared with other long-term multi-day snow cover products, such as weekly NHSCE.

4.2. Comparisons with fine-resolution MCD10A1-TP

Subject to the spatial coverage and time span of MCD10A1-TP, the comparison between TPSCE and fine-resolution MCD10A1-TP was confined to the overlap regions. The climatology of and changes in SCF calculated from the TPSCE and MCD10A1-TP for the period 2001–2014

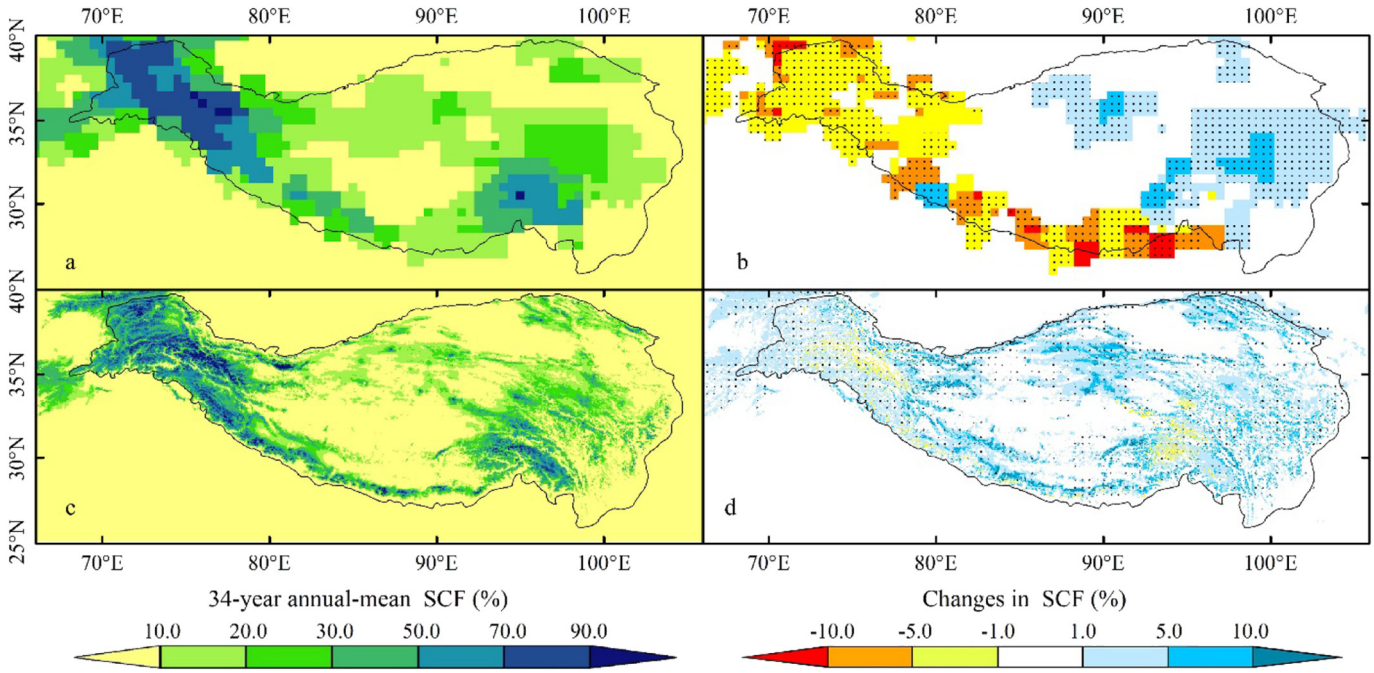

Fig. 12. 34-year climatology of annual-mean SCF (%) across the TP for the period 1982–2015 (excluding 1994), calculated from (a) NHSCE and (c) TPSCE. The 34-year changes in SCF (%) were calculated from (b) NHSCE and (d) TPSCE. Black dots in (b) and (d) indicate changes that are significant at the 95% level.

across the TP are shown in Fig. 10. In this study, the changes are expressed as linear trends multiplied by the time interval.

The spatial distributions of the SCF climatology derived from MCD10A1-TP (Fig. 10(a)) and the TPSCE (Fig. 10(c)) are similar during 2001–2014, with high SCF values distributed mainly in the upper reaches of the Tarim, Indus, Brahmaputra, Salween, and Mekong River basins, and the low SCF values distributed in the Inner TP and Qaidam River basins. However, compared with the MCD10A1-TP-derived SCF maps, the SCF values in the high-altitude southern margin of the Brahmaputra River basin and the western Pamir regions were overestimated in the TPSCE SCF maps. This overestimation was caused mainly by a relatively low spatial resolution in the newly developed TPSCE data set, resulting in overestimated (underestimated) SCF values in regions with heavy (low) snow distribution. In addition, both MCD10A1-TP and TPSCE are generated by integrating optical and passive microwave snow data. Thus, uncertainties in the MCD10A1-TP and TPSCE caused by coarse spatial resolution of passive microwave remote sensing, ground temperature, snow characteristics and topography (Dai et al., 2017; Tsutsui and Koike, 2012) may also result in the discrepancies between MCD10A1-TP and TPSCE.

Variations in SCF derived from MCD10A1-TP (Fig. 10(b)) and TPSCE (Fig. 10(d)) show marked spatial differences from 2001 through 2014. Compared with the changes calculated from MCD10A1-TP, SCF increased not only in the upper reaches of the Yangtze, Mekong, and Brahmaputra River basins, but also in the northern Inner TP river basins, as shown in the change maps calculated from the TPSCE. Since the changes calculated from MCD10A1-TP and TPSCE for the period 2001–2014 are not statistically significant, as indicated in Fig. 10(b) and (d), owing to the short time interval, we do not present a detailed analysis of the spatial differences in this study. However, to explore the detail of the similarities and differences between MCD10A1-TP and TPSCE, we summarize the comparisons between the annual-mean SCF calculated from MCD10A1-TP and TPSCE for each basin (Fig. 11), with the RMSE and bias listed in Table 7.

The annual-mean SCF calculated from MCD10A1-TP and TPSCE generally shows positive linear correlations across the entire region and each basin for the period 2001–2014 (Fig. 11), with a maximum correlation coefficient ($r = 0.85, p < 0.05$) in the Mekong River basin and a minimum correlation coefficient ($r = 0.12, p > 0.05$) in the Inner TP river basins. For basins with snow distribution (e.g., Indus, Mekong, and Salween), the TPSCE could capture the snow information adequately. However, subject to a 5-km spatial resolution, the TPSCE could not identify snow cover grid cells accurately in sparse snow cover regions (e.g., Inner TP and Qaidam).

As shown in Table 7, we found large differences in RMSE and bias among the basins across the TP for the period 2001–2014. The RMSE between the TPSCE SCF series and the MCD10A1-TP SCF series was 2.15% over the entire TP during the period, ranging from 0.64% in the Ganges River basin to 3.79% in the Salween River basin. In addition, the bias between the TPSCE SCF series and the MCD10A1-TP SCF series over the entire TP for the period was −0.25%, with a maximum underestimated SCF (−2.80%) in the Salween River basin and a maximum overestimated SCF (1.52%) in the Qaidam River basin.

5. Cross-comparison between snow cover from TPSCE and other climate variables

5.1. Long-term snow cover changes derived from TPSCE

The long-term snow cover changes derived from the TPSCE and NHSCE from 1982 to 2015 were compared. To match the temporal resolution of the weekly NHSCE data set, the aggregated weekly TPSCE were used. The climatology and changes in SCF derived from the NHSCE and TPSCE data sets across the TP for the period 1982–2015 are presented in Fig. 12. Because the time series of the TPSCE is incomplete due to data missing of AVHRR surface reflectance in 1994, we excluded this year in detection of long-term changes in snow cover and cross-comparisons with other climate variables in this study.

The 34-year climatology of the annual-mean SCF calculated from NHSCE (Fig. 12(a)) and TPSCE (Fig. 12(c)) is similar in spatial distribution during 1982–2015. However, the climatology of the annual-mean SCF calculated from the TPSCE demonstrates more detailed information on long-term SCF conditions across the TP. Compared with the SCF maps calculated from TPSCE, the SCF values in the southeast Brahmaputra River basins and northwest Pamirs were overestimated in the NHSCE SCF maps. In addition to the low spatial resolution of the

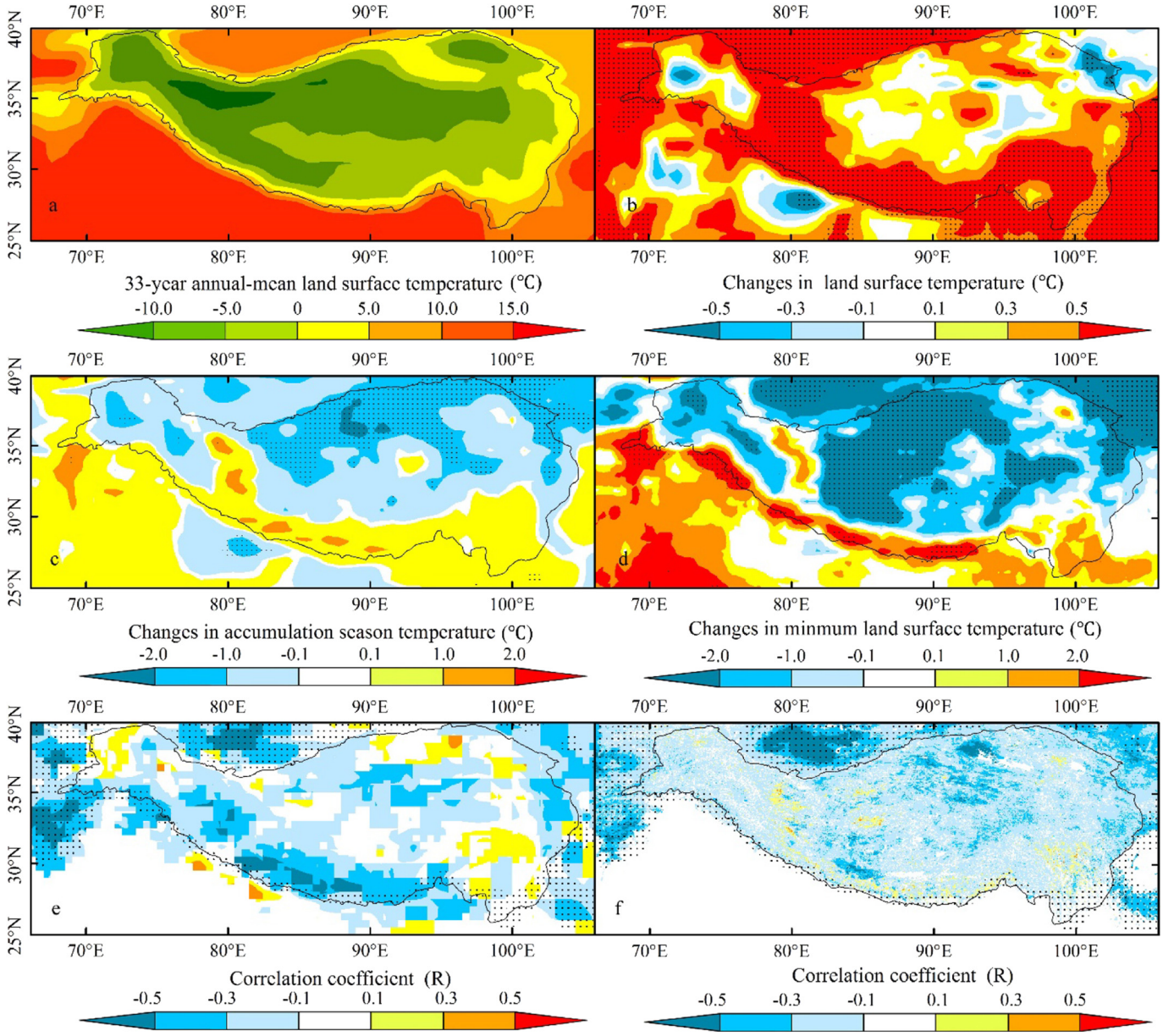

Fig. 13. 33-year (a) climatology of annual-mean land surface temperature (°C) and changes in (b) annual-mean land surface temperature (°C), (c) accumulation season temperature, and (d) minimum land surface temperature across the TP for the period 1982–2016 (excluding 1994). The correlation coefficient (*R*) between land surface temperature and SCF calculated from (e) NHSCE and (f) TPSCE snow cover products. Black dots in (b), (c), and (d) indicate that changes are significant at the 95% level. Black dots in (e) and (f) indicate that the correlation coefficients are statistically significant at the 95% level.

NHSCE snow cover products, the definition of snow cover in the NHSCE snow cover products also contributes to this deviation. According to Helfrich et al. (2007) and Brown and Robinson (2011), the grid cell was marked as 0 or 1 in the NHSCE snow cover products, with < 50% or ≥50% snow occurrence probability, respectively. This definition of snow cover in the NHSCE data set could result in overestimated SCF values in regions with heavy snow but underestimated SCF values in regions with patchy snow. This is because NHSCE could only detect grid cells with ≥50% snow occurrence probability effectively, whereas the patchy snow could not be identified well.

The response of SCF to climate change can be demonstrated well by long-term SCF changes. Variations in SCF calculated from NHSCE (Fig. 12(b)) and TPSCE (Fig. 12(d)) show large spatial differences across the TP during 1982–2015, especially in the Pamirs and the southern margin of the TP. In contrast with a significant SCF decrease in the Brahmaputra River basin, as shown in Fig. 12(b), the SCF increases in most areas of the Brahmaputra River basin, as shown in Fig. 12(d). Climatic variables, including temperature and precipitation, were considered the contributing factors to these SCF changes. However, previous studies focused mainly on snow cover changes in northern high latitudes, with the actual conditions of snow cover and the driving forces in mid-latitudes over a long time span discussed only rarely. To solve the lack of references in evaluating the reliability of long-term NHSCE and TPSCE, we conducted cross-comparison as discussed in the following sections.

5.2. Cross-comparison between snow cover and land surface temperature

The cross-comparison between SCF and land surface temperature during 1982–2016 was conducted (Fig. 13). Based on the annual cycle of SCF over the TP from 2001 to 2014 (Chen et al., 2017), snow cover increased from September to February, with SCF increasing

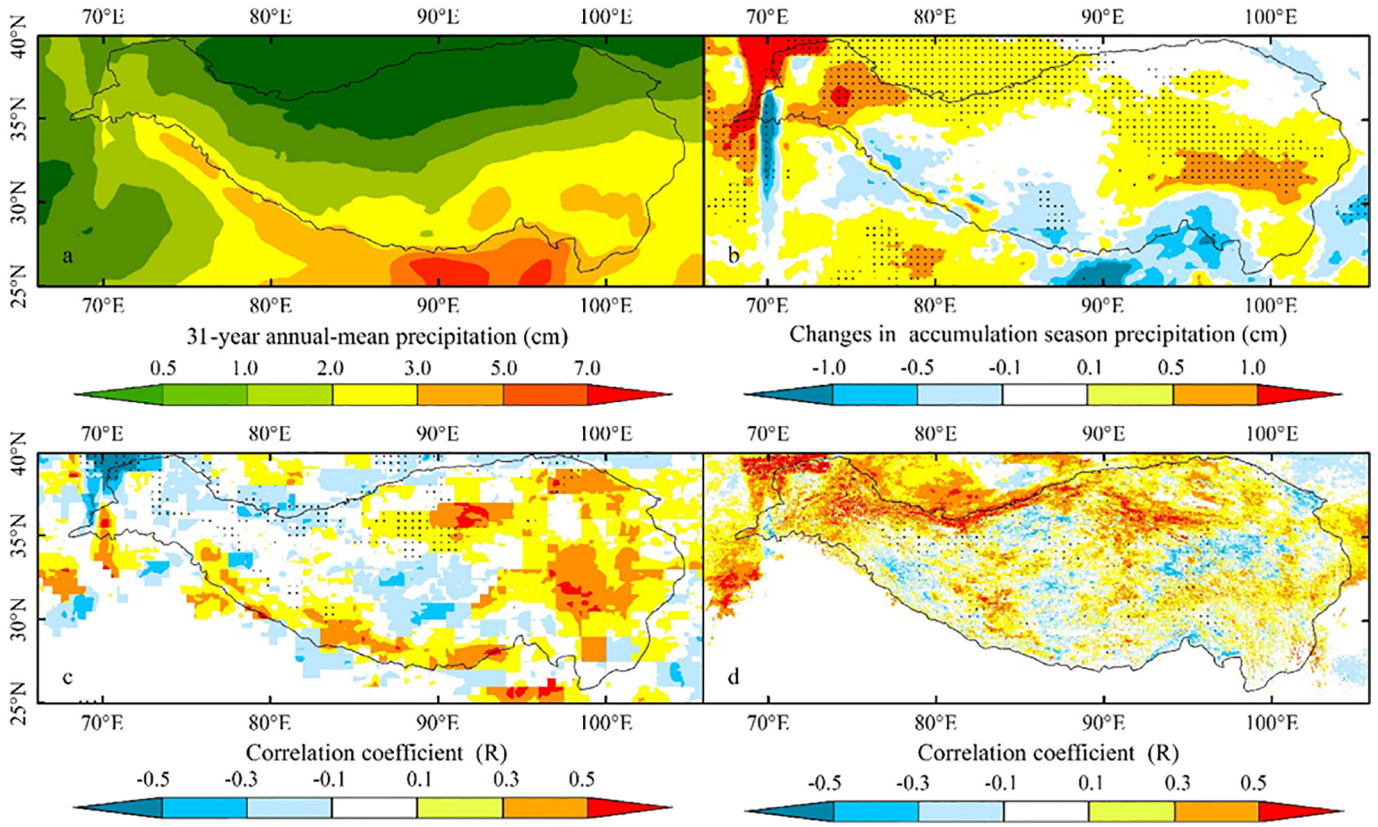

Fig. 14. 31-year (a) climatology of annual-mean precipitation (cm) and (b) changes in accumulation season precipitation across the TP for the period 1983–2015 (excluding 1994). The correlation coefficient (*R*) between accumulation season precipitation and SCF is calculated from (c) NHSCE and (d) TPSCE snow cover products. Black dots in (b) indicate that changes are significant at the 95% level. Black dots in (c) and (d) indicate that the correlation coefficient is statistically significant at the 95% level.

significantly in December and January. To compare the changes in temperature and SCF, this study used the December–January average accumulation season temperature and the minimum temperature.

As shown in Fig. 13(b), the 33-year annual-mean land surface temperature shows a warmer trend in most of the regions across the TP for the period 1982–2016 (excluding 1994). However, in contrast with the changes in the annual-mean temperature, both accumulation season temperature (Fig. 13(c)) and minimum temperature (Fig. 13(d)) show a generally cooler trend across the TP during 1982–2016 (excluding 1994). This is beneficial to snow accumulation on the ground and could have resulted in longer-duration snow cover and increased SCF. The cooler accumulation season temperature and the lower minimum temperature across the TP are consistent partly with the long-term tendency of large-scale cooling trends in land surface temperature during winter over mid-latitudes that have been observed since approximately the 1990s (Cohen et al., 2014; Cohen et al., 2012).

Maps of the correlation between the accumulation season temperature and NHSCE and the TPSCE are shown in Fig. 13(e) and 13(f), respectively. A generally negative correlation between the accumulation season temperature and SCF is indicated for most regions of the study area, as shown in Fig. 13(e) and (f). However, the TPSCE provides superior results in the Pamirs because of the erroneous positive correlation between the accumulation season temperature and SCF calculated from the NHSCE. Meanwhile, in the south margin of the TP with high annual-mean SCF, the NHSCE provides better correlation with accumulation season temperature compared with the TPSCE.

5.3. Cross-comparison between snow cover and accumulation season precipitation

In addition to the accumulation season temperature, precipitation plays a critical role in snow accumulation on the ground. The cross-comparison between snow cover and accumulation season precipitation during 1983–2015 was conducted (Fig. 14). As shown in Fig. 14(b), accumulation season precipitation increases in most of the central and eastern TP during 1983–2015 (excluding 1994), which is beneficial to snow accumulation on the ground and could have resulted in deeper snow cover and a longer snow season. This pattern coincides with the previous findings on large-scale cold snaps, heavy snowfall, and glacier events at middle latitudes since the 1990s (Cohen et al., 2010; Cohen et al., 2012; Yao et al., 2012). Furthermore, the SCF was shown to be correlated positively with the accumulation season precipitation, as demonstrated in Fig. 14(c) and (d). Compared with Fig. 14(d), the correlation between the accumulation season precipitation and SCF derived from the NHSCE (Fig. 14(c)) shows poor results in the western TP and, particularly, the Pamirs. However, in the eastern and southern margins of the TP, the performance of the NHSCE is better than the TPSCE.

5.4. Cross-comparison between snow cover and land surface albedo

Land surface albedo has been shown to be related closely with snow cover changes because of the highly reflective surface of snow cover. The cross-comparison between snow cover and land surface albedo during 1982–2015 was conducted. The 32-year climatology of the annual-mean land surface albedo and changes across the TP for the period 1982–2015 (excluding 1994) calculated from the CLARA-SAL are shown in Fig. 15.

The distribution of 32-year annual-mean land surface albedo across the TP from 1982 to 2015 (excluding 1994) (Fig. 15(a)) is similar to the climatology of the annual-mean SCF distribution shown in Fig. 12. Moreover, changes in land surface albedo partly represent snow cover

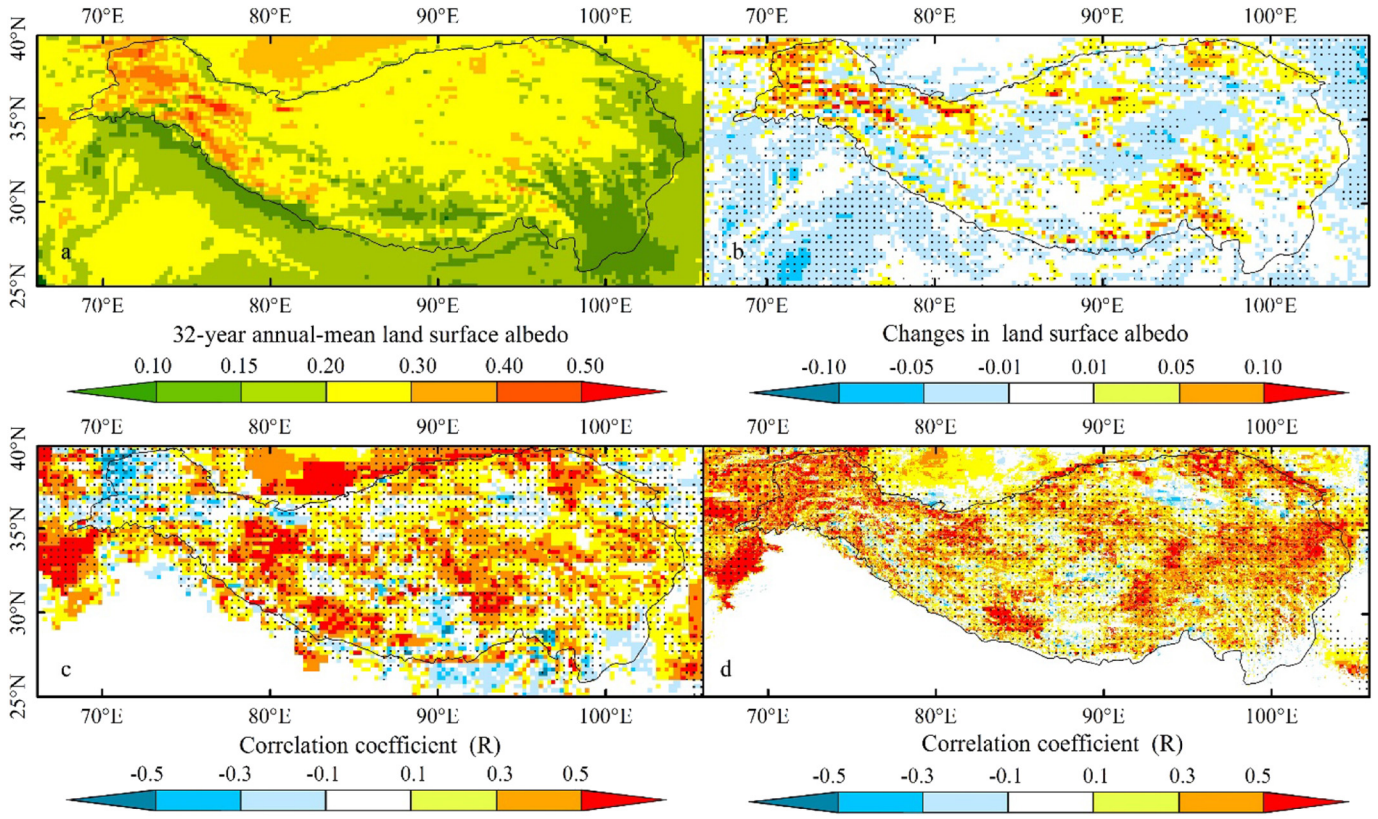

Fig. 15. 32-year (a) climatology of annual-mean land surface albedo and (b) changes across the TP for the period 1982–2015 (excluding 1994). The correlation coefficient (*R*) between land surface albedo and SCF was calculated from (c) NHSCE and (d) TPSCE snow cover products. Black dots in (b) indicate that changes are significant at the 95% level. Black dots in (c) and (d) indicate that the correlation coefficient is statistically significant at the 95% level.

changes according to Chen et al. (2017). As shown in Fig. 15(b), the land surface albedo shows an increasing trend in the Pamirs and Brahmaputra River basin, which is the opposite of the decreasing SCF calculated from the NHSCE snow cover maps (Fig. 12(b)). Moreover, compared with Fig. 15(c), the correlation coefficients between the land surface albedo and SCF calculated from the TPSCF were more reasonable, especially in the Pamirs. By comparison with long-term changes in temperature, precipitation, and land surface albedo, we found that the performance of the newly developed TPSCE is superior compared with that of the widely used NHSCE snow cover products in capturing long-term snow cover anomalies across the TP.

6. Summary and conclusion

The long-term snow cover condition across the TP has not been well documented owing to limited data availability. Using AVHRR surface reflectance CDR and several existing snow cover products, we generate a composite daily SCE record of the TP from 1981 to 2016. The newly developed TPSCE has several advantages in TP snow cover studies, including long time series, high and temporal spatial resolution, and complete spatial coverage, compared with NHSCE and GlobSnow with low spatial resolution, Suomi-NPP and MODIS with short time span, and JASMES with incomplete coverage. This data set facilitates a novel report on the evolution of snow cover across the TP during three decades (1981 to 2016) as a peculiar mid-latitude cryosphere.

Validation results of the daily TPSCE against ground snow-depth observations and the fine-resolution MCD10A1-TP snow cover show high snow discrimination accuracy of the TPSCE. Comparisons of SCF distribution and historical change analysis across the entire TP and nine river basins (e.g. Brahmaputra, Ganges, Hexi, Indus, Mekong, Qaidam, Salween, Tarim, Yangtze, Yellow, and Inner TP) from 2001 to 2014 provide the RMSE and bias between the newly developed TPSCE and the fine-resolution MCD10A1-TP in SCF quantification over the TP, and show that the TPSCE could capture snow distribution skillfully. The cross-comparisons between the SCF anomaly derived from the TPSCE and changes in land surface temperature, precipitation, and albedo further show the reliability of the newly developed TPSCE data set. Compared with the correlation between the SCF calculated from the NHSCE data set and the land surface temperature, precipitation, and albedo, the SCF calculated from the TPSCE presents a superior performance.

This long-term composite snow cover data set is suited for studying seasonal snow cover across the TP and could present a unique opportunity for climatological and hydrological studies on seasonal snow cover and surface water resource changes in the TP over the past three decades. However, some issues remain in the newly developed TPSCE data set, such as lower confidence of snow cover before 2000 compared with that after 2000, few ground snow-depth observations in regions with heavy snow distribution, and a confined study area limited by the availability of ancillary data. Cloud contamination is one of the most difficult aspects in snow cover discrimination when using optical remote sensing images. However, with the utility of historical passive microwave images and the development of the cloud detection approach, long-term, high-quality, and fine-resolution snow cover products are expected in the future.

Acknowledgements

This study was funded by the National Natural Science Foundation of China (under grant No. 91547210, No. 51722903, and No. 91437214), the National Key Research and Development Program of China (under grant No. 2016YFE0102400 and 2016YFA0600103), and China Postdoctoral Science Foundation (under grant No. 2016M600080). All colleagues involved in producing this data set are

highly appreciated. The AVHRR surface reflectance CDR and the PERSIANN precipitation CDR are available at the National Climatic Data Center (https://www.ncdc.noaa.gov/). The MCD10A1-TP snow cover products are provided by the Northwest Institute of Eco-Environment and Resources, Chinese Academy of Sciences (http://westdc.westgis.ac.cn/data). The MODIS, NHSCE, and IMS snow cover products are obtained from the National Snow and Ice Data Centre (http://nsidc.org/data/G02156). The JASMES snow cover products are obtained from the Japan Aerospace Exploration Agency (http://kuroshio.eorc.jaxa.jp/JASMES/datalist.html). The ERA-Interim temperature data sets are available at the European Centre for Medium-Range Weather Forecasts (https://www.ecmwf.int/). The MCD12Q1 land cover products are available at the LAND Processes Distributed Active Archive Centre (https://lpdaac.usgs.gov/). The SRTM DEM is available at http://seamless.usgs.gov/. The ground observations are available at the Meteorological Data Centre of the China Meteorological Administration (http://data.cma.cn/). Reviewers and editors' comments that are valuable for improving this study and manuscript are acknowledged. The TPSCE data set generated from this study is available upon reasonable request (dlong@tsinghua.edu.cn).

References

Ashouri, H., Hsu, K.-L., Sorooshian, S., Braithwaite, D.K., Knapp, K.R., Cecil, L.D., Nelson, B.R., Prat, O.P., 2015. PERSIANN-CDR: daily precipitation climate data record from multisatellite observations for hydrological and climate studies. Bull. Am. Meteorol. Soc. 96, 69–83. http://dx.doi.org/10.1175/BAMS-D-13-00068.1.

Brown, R.D., Robinson, D.A., 2011. Northern Hemisphere spring snow cover variability and change over 1922–2010 including an assessment of uncertainty. Cryosphere 5, 219–229. http://dx.doi.org/10.5194/tc-5-219-2011.

Brown, R., Derksen, C., Wang, L., 2010. A multi-data set analysis of variability and change in Arctic spring snow cover extent, 1967–2008. J. Geophys. Res. Atmos. 115, D16111.

Che, T., Li, X., Jin, R., Armstrong, R., Zhang, T., 2008. Snow depth derived from passive microwave remote-sensing data in China. Ann. Glaciol. 145–154.

Chen, C., Lakhankar, T., Romanov, P., Helfrich, S., Powell, A., Khanbilvardi, R., 2012. Validation of NOAA-Interactive Multisensor Snow and Ice Mapping System (IMS) by comparison with ground-based measurements over continental United States. Remote Sens. 4, 1134–1145.

Chen, X., Liang, S., Cao, Y., He, T., Wang, D., 2015. Observed contrast changes in snow cover phenology in northern middle and high latitudes from 2001–2014. Sci. Rep. 5, 16820.

Chen, X., Long, D., Hong, Y., Liang, S., Hou, A., 2017. Observed radiative cooling over the Tibetan Plateau for the past three decades driven by snow-cover-induced surface albedo anomaly. J. Geophys. Res. Atmos. 122, 6170–6185.

Cohen, J., Foster, J., Barlow, M., Saito, K., Jones, J., 2010. Winter 2009–2010: a case study of an extreme Arctic Oscillation event. Geophys. Res. Lett. 37, 2010GL044256.

Cohen, J.L., Furtado, J.C., Barlow, M.A., Alexeev, V.A., Cherry, J.E., 2012. Arctic warming, increasing snow cover and widespread boreal winter cooling. Environ. Res. Lett. 7, 014007.

Cohen, J., Screen, J.A., Furtado, J.C., Barlow, M., Whittleston, D., Coumou, D., Francis, J., Dethloff, K., Entekhabi, D., Overland, J., Jones, J., 2014. Recent Arctic amplification and extreme mid-latitude weather. Nat. Geosci. 7, 627–637.

Dai, L., Che, T., Ding, Y., Hao, X., 2017. Evaluation of snow cover and snow depth on the Qinghai–Tibetan Plateau derived from passive microwave remote sensing. Cryosphere 11, 1933–1948.

Dee, D.P., Uppala, S.M., Simmons, A.J., Berrisford, P., Poli, P., Kobayashi, S., Andrae, U., Balmaseda, M.A., Balsamo, G., Bauer, P., Bechtold, P., Beljaars, A.C.M., van de Berg, L., Bidlot, J., Bormann, N., Delsol, C., Dragani, R., Fuentes, M., Geer, A.J., Haimberger, L., Healy, S.B., Hersbach, H., Hólm, E.V., Isaksen, L., Kållberg, P., Köhler, M., Matricardi, M., McNally, A.P., Monge-Sanz, B.M., Morcrette, J.J., Park, B.K., Peubey, C., de Rosnay, P., Tavolato, C., Thépaut, J.N., Vitart, F., 2011. The ERA-interim reanalysis: configuration and performance of the data assimilation system. Q. J. R. Meteorol. Soc. 137, 553–597.

Dong, J., Zhang, G., Zhang, Y., Xiao, X., 2013. Reply to Wang et al.: snow cover and air temperature affect the rate of changes in spring phenology in the Tibetan Plateau. Proc. Natl. Acad. Sci. U. S. A. 110, E2856–E2857.

Franch, B., Vermote, E., Roger, J.-C., Murphy, E., Becker-Reshef, I., Justice, C., Claverie, M., Nagol, J., Csiszar, I., Meyer, D., Baret, F., Masuoka, E., Wolfe, R., Devadiga, S., 2017. A 30+ year AVHRR land surface reflectance climate data record and its application to wheat yield monitoring. Remote Sens. 9, 296.

Frei, A., Tedesco, M., Lee, S., Foster, J., Hall, D.K., Kelly, R., Robinson, D.A., 2012. A review of global satellite-derived snow products. Adv. Space Res. 50, 1007–1029. http://dx.doi.org/10.1016/j.asr.2011.12.021.

Friedl, M.A., Sulla-Menashe, D., Tan, B., Schneider, A., Ramankutty, N., Sibley, A., Huang, X., 2010. MODIS collection 5 global land cover: algorithm refinements and characterization of new datasets. Remote Sens. Environ. 114, 168–182. http://dx.doi.org/10.1016/j.rse.2009.08.016.

Gao, L., Hao, L., Chen, X.-w., 2014. Evaluation of ERA-interim monthly temperature data over the Tibetan Plateau. J. Mt. Sci. 11, 1154–1168.

Hall, D.K., Riggs, G.A., 2007. Accuracy assessment of the MODIS snow products. Hydrol. Process. 21, 1534–1547.

Hall, D.K., Riggs, G.A., Salomonson, V.V., 1995. Development of methods for mapping global snow cover using Moderate Resolution Imaging Spectroradiometer Data. Remote Sens. Environ. 54, 127–140. http://dx.doi.org/10.1016/0034-4257(95)00137-P.

Hall, D.K., Riggs, G.A., Salomonson, V.V., DiGirolamo, N.E., Bayr, K.J., 2002. MODIS snow-cover products. Remote Sens. Environ. 83, 181–194.

Hansen, J., Ruedy, R., Sato, M., Lo, K., 2010. Global surface temperature change. Rev. Geophys. 48, RG4004.

Helfrich, S.R., McNamara, D., Ramsay, B.H., Baldwin, T., Kasheta, T., 2007. Enhancements to, and forthcoming developments in the Interactive Multisensor Snow and Ice Mapping System (IMS). Hydrol. Process. 21, 1576–1586.

Hori, M., Sugiura, K., Kobayashi, K., Aoki, T., Tanikawa, T., Kuchiki, K., Niwano, M., Enomoto, H., 2017. A 38-year (1978–2015) Northern Hemisphere daily snow cover extent product derived using consistent objective criteria from satellite-borne optical sensors. Remote Sens. Environ. 191, 402–418. http://dx.doi.org/10.1016/j.rse.2017.01.023.

Huang, X., Hao, X., Feng, Q., Wang, W., Liang, T., 2014. A new MODIS daily cloud free snow cover mapping algorithm on the Tibetan Plateau. Sci. Cold Arid. Reg. 6, 0116–0123.

Kang, S., Xu, Y., You, Q., Flügel, W.-A., Pepin, N., Yao, T., 2010. Review of climate and cryospheric change in the Tibetan Plateau. Environ. Res. Lett. 5, 015101.

Kelly, R.E., Chang, A.T., Tsang, L., Foster, J.L., 2003. A prototype AMSR-E global snow area and snow depth algorithm. IEEE Trans. Geosci. Remote Sens. 41, 230–242.

Key, J.R., Mahoney, R., Liu, Y., Romanov, P., Tschudi, M., Appel, I., Maslanik, J., Baldwin, D., Wang, X., Meade, P., 2013. Snow and ice products from Suomi NPP VIIRS. J. Geophys. Res. Atmos. 118, 12,816–812,830.

Khlopenkov, K.V., Trishchenko, A.P., 2007. SPARC: new cloud, snow, and cloud shadow detection scheme for historical 1-km AVHRR data over Canada. J. Atmos. Ocean. Technol. 24, 322–343. http://dx.doi.org/10.1175/JTECH1987.1.

Kidder, S.Q., 1987. A multispectral study of the St. Louis area under snow-covered conditions using NOAA-7 AVHRR data. Remote Sens. Environ. 22, 159–172. http://dx.doi.org/10.1016/0034-4257(87)90056-3.

Larson, C., 2011. 'Third pole' glacier research gets a boost from China. Science 334, 1199.

Ma, Y., Wang, Y., Wu, R., Hu, Z., Yang, K., Li, M., Ma, W., Zhong, L., Sun, F., Chen, X., Zhu, Z., Wang, S., H., I., 2009. Recent advances on the study of atmosphere-land interaction observations on the Tibetan Plateau. Hydrol. Earth Syst. Sci. 13, 1103–1111. http://dx.doi.org/10.5194/hess-13-1103-2009.

Polashenski, C.M., Dibb, J.E., Flanner, M.G., Chen, J.Y., Courville, Z.R., Lai, A.M., Schauer, J.J., Shafer, M.M., Bergin, M., 2015. Neither dust nor black carbon causing apparent albedo decline in Greenland's dry snow zone: implications for MODIS C5 surface reflectance. Geophys. Res. Lett. 42, 9319–9327.

Pu, Z., Xu, L., Salomonson, V.V., 2008. MODIS/Terra observed snow cover over the Tibet Plateau: distribution, variation and possible connection with the East Asian Summer Monsoon (EASM). Theor. Appl. Climatol. 97, 265–278.

Pulliainen, J., 2010. In: Overview on GlobSnow Project: key questions to be resolved (coverage, aggregation, validation, towards a future ECV). The 1st ESA DUE GlobSnow User Workshop, Innsbruck, Austria.

Qian, Y., Flanner, M.G., Leung, L.R., Wang, W., 2011. Sensitivity studies on the impacts of Tibetan Plateau snowpack pollution on the Asian hydrological cycle and monsoon climate. Atmos. Chem. Phys. 11, 1929–1948. http://dx.doi.org/10.5194/acp-11-1929-2011.

Qu, X., Hall, A., 2014. On the persistent spread in snow-albedo feedback. Clim. Dyn. 42, 69–81.

Riihelä, A., Manninen, T., Laine, V., Andersson, K., Kaspar, F., 2013. CLARA-SAL: a global 28 yr timeseries of Earth's black-sky surface albedo. Atmos. Chem. Phys. 13, 3743–3762. http://dx.doi.org/10.5194/acp-13-3743-2013.

Robinson, D.A., Dewey, K.F., Richard, R., Heim, J., 1993. Global snow cover monitoring: an update. Bull. Am. Meteorol. Soc. 74, 1689–1696. http://dx.doi.org/10.1175/1520-0477(1993)074<1689:GSCMAU>2.0.CO;2.

Tsutsui, H., Koike, T., 2012. Development of snow retrieval algorithm using AMSR-E for the BJ ground-based station on seasonally frozen ground at low altitude on the Tibetan Plateau. J. Meteorol. Soc. Jpn. 90, 99–112.

Vermote, E., Justice, C., Csiszar, I., Eidenshink, J., Myneni, R., Baret, F., Masuoka, E., Wolfe, R., Claverie, M., NOAA CDR Program, 2014. NOAA Climate Data Record (CDR) of AVHRR Surface Reflectance, Version 4. NOAA National Climatic Data Centerhttp://dx.doi.org/10.7289/V5TM782M.

Wu, Z., Jiang, Z., Li, J., Zhong, S., Wang, L., 2012. Possible association of the western Tibetan Plateau snow cover with the decadal to interdecadal variations of northern China heatwave frequency. Clim. Dyn. 39, 2393–2402.

Yao, T., Thompson, L., Yang, W., Yu, W., Gao, Y., Guo, X., Yang, X., Duan, K., Zhao, H., Xu, B., Pu, J., Lu, A., Xiang, Y., Kattel, D.B., Joswiak, D., 2012. Different glacier status with atmospheric circulations in Tibetan Plateau and surroundings. Nat. Clim. Chang. 2, 663–667.

Yu, J., Zhang, G., Yao, T., Xie, H., Zhang, H., Ke, C., Yao, R., 2016. Developing daily cloud-free snow composite products from MODIS Terra–Aqua and IMS for the Tibetan Plateau. IEEE Trans. Geosci. Remote Sens. 54, 2171–2180.

Zhou, H., Aizen, E., Aizen, V., 2013. Deriving long term snow cover extent dataset from AVHRR and MODIS data: Central Asia case study. Remote Sens. Environ. 136, 146–162. http://dx.doi.org/10.1016/j.rse.2013.04.015.